A 3-D extension of the Multiscale Control Volume method for the simulation of the single-phase flow in anisotropic and heterogeneous porous media

Cumaru Silva Alves, Filipe Antônio; de Souza, Artur Castiel Reis; Lyra, Paulo Roberto Maciel; de Carvalho, Darlan Karlo Elisiário

DOI
10.1016/j.apm.2024.05.045

Publication date
2024

Document Version
Final published version

Published in
Applied Mathematical Modelling

Citation (APA)
Cumaru Silva Alves, F. A., de Souza, A. C. R., Lyra, P. R. M., & de Carvalho, D. K. E. (2024). A 3-D extension of the Multiscale Control Volume method for the simulation of the single-phase flow in anisotropic and heterogeneous porous media. *Applied Mathematical Modelling*, *134*, 198-222. https://doi.org/10.1016/j.apm.2024.05.045

Applied Mathematical Modelling 134 (2024) 198–222

Contents lists available at ScienceDirect

Applied Mathematical Modelling

journal homepage: www.elsevier.com/locate/apm

A 3-D extension of the Multiscale Control Volume method for the simulation of the single-phase flow in anisotropic and heterogeneous porous media

Filipe Antônio Cumaru Silva Alves [a,b,*], Artur Castiel Reis de Souza [b], Paulo Roberto Maciel Lyra [a], Darlan Karlo Elisiário de Carvalho [a]

[a] Civil Engineering Graduate Program, Universidade Federal de Pernambuco, Av. da Arquitetura, S/N, Recife, CEP 50740-550, Brazil
[b] Delft Institute of Applied Mathematics, Delft University of Technology, Mekelweg 4, Delft, 2628CD, the Netherlands

ARTICLE INFO

Keywords:
MsCV
MPFA-D
GLS
Background grid
Single-phase flow

ABSTRACT

The level of detail on modern geological models requires higher resolution grids that may render the simulation of multiphase flow in porous media intractable. Moreover, these models may comprise highly heterogeneous media with phenomena taking place in different scales. Scale transferring techniques allow for the solution of such problems in a lower resolution scale at reduced computational cost. Among these techniques, the Multiscale Finite Volume (MsFV) method constructs a set of numerical operators in order to map quantities from the fine-scale mesh to a coarser one and vice-versa while maintaining flux conservation on both scales. However, the MsFV formulation, as originally stated, is only consistent on k-orthogonal grids since it uses a linear Two-point Flux Approximation (TPFA) method and may struggle to generate consistent primal-dual coarse grids pairs on unstructured grids. The Multiscale Restriction Smoothed-Basis method (MsRSB) improves on the MsFV by introducing a new iterative procedure to find the multiscale operators and the concept of support regions which reduces the method's complexity when applied to unstructured fine and coarse grids. The original version was only consistent on k-orthogonal fine grids due to the TPFA discretization, but filtering methods have been developed to also enable consistent multipoint schemes on the fine scale. Meanwhile, the Multiscale Control Volume method (MsCV) replaces the TPFA by the Multipoint Flux Approximation with a Diamond stencil (MPFA-D) scheme on the fine-scale while further enhancing the generation of the geometric entities to allow unstructured grids on the fine and coarse scales for two-dimensional simulations. In this work we propose an extension to three-dimensional geometries of both the MsCV and the algorithm to obtain the multiscale geometric entities based on the concept of a background grid, a coarser grid used as a proxy for the primal coarse grid. We modify the original MPFA-D method to use the very robust Global Least Squares (GLS) interpolation technique to obtain the required auxiliary nodal unknowns. We also introduce an enhanced version of the 3-D MsCV with the incorporation of the enhanced MsRSB (E-MsRSB) to enforce M-matrix properties and improve convergence. Finally, we employ the MsCV operators in a two-stage smoother to show how it can be used as a good iterative procedure to recover the fine-scale solution. We show that the 3-D MsCV method produces good results employing unstructured grids on both scales to handle the simulation of the single-phase flow in anisotropic, and heterogeneous porous media

* Corresponding author at: Delft Institute of Applied Mathematics, Delft University of Technology, Mekelweg 4, Delft, 2628CD, the Netherlands.
E-mail address: filipe.cumaru@ufpe.br (F.A. Cumaru Silva Alves).

https://doi.org/10.1016/j.apm.2024.05.045
Received 5 July 2023; Received in revised form 16 May 2024; Accepted 31 May 2024

Available online 7 June 2024

and that the smoothing procedure is able to accurately retrieve the fine-scale solution within a few iterations.

1. Introduction

The numerical simulation of the fluid flow in porous media is a computationally expensive task. On top of the difficulty in modelling such phenomena, the size of the discrete models can quickly render the problem intractable for conventional methods and hardware [1–3]. In order to reduce the computational complexity, scale transferring such as upscaling and multiscale can be applied. Whereas upscaling relies on a homogenization procedure to map the original problem to a lower resolution scale [4], multiscale methods compute basis functions as the solution of locally defined reduced boundary conditions problems, which in turn allow to reconstruct an approximate solution on the original high resolution or fine scale [5].

Among the proposed multiscale formulations, we turn our attention to the Multiscale Finite Volume (MsFV) method introduced by [6] in the context of subsurface flow simulation. In this approach, an auxiliary dual coarse grid is employed in order to define the operators by solving local problems in this grid. Many improvements have since been proposed to the MsFV such as the introduction of more complex physics to the model in [7,8] and an algebraic formulation of the MsFV by [9,10].

Most of the formulations in the MsFV family are not consistent on general coarse and fine-scale grids. This is mainly due to the usage of a Two-point Flux Approximation scheme (TPFA) on the fine-scale, which is only consistent on k-orthogonal grids [11], and the difficulty of generating the multiscale entities in unstructured geometries [12–14]. Previous works, such as [15], have proposed formulations for the MsFV based on CVD-MPFA schemes (Control Volume Distributed Multipoint Flux Approximation) in two dimensions, showing the gains when applied to non-K-orthogonal grids. The Multiscale Restriction-Smoothed Basis (MsRSB) [16] provides a new way to compute the basis functions via an iterative procedure and eliminates the use of an explicit primal or dual grids by using support regions, which reduces the complexity in the application to unstructured grids for the simulation of the multiphase flow in black-oil and compositional models in two and three dimensions [17]. However, the MsRSB still relies on the TPFA for the discretization on the fine-scale, resulting in inconsistencies when applied to general unstructured grids. This issue is addressed in [18] where an extension of the MsRSB for non M-matrices is introduced, the enhanced MsRSB (E-MsRSB), by designing a preconditioner that filters all non-positive off-diagonal terms from the system matrix. Souza et al. [14] presented the Multiscale Control Volume (MsCV) which improves on the original MsRSB by replacing the TPFA with the Multipoint Flux Approximation with a diamond stencil (MPFA-D) scheme from [19] and [20], hence providing a consistent flux approximation for unstructured grids on both scales in the context of the simulation of the 2-D two-phase flow in porous media.

A consistent flux approximation on non-k-orthogonal grids is key as the application of the TPFA in such cases does not fully capture the tangential components of the Darcy flow, yielding unphysical artificial numerical diffusion [21,22]. In addition, since the multiscale approximation can only be as good as the fine-scale reference solution, employing MPFA methods in such context guarantees that the latter will indeed reproduce the flow phenomena in its entirety when coupled with an iterative solver. It is worth pointing out that linear MPFA schemes do not guarantee that the Discrete Maximum Principle (DMP) is always satisfied. Nevertheless, non-linear repair techniques can still be applied to reduce or suppress such effects, as seen in [23,24].

The MPFA-D, like other MPFA variants [25,26], requires the interpolation of the nodal unknowns involved in its flux expression. The choice of the interpolation strategy is crucial and deeply affects the convergence of the method. In its 3-D formulation, as described by [27], the Linearity-Preserving Explicit Weight (LPEW3) interpolation is adopted. Although it observes the Linearity-Preserving Criterion (LPC), it fails to compute accurate solutions in the presence of strong anisotropy. To overcome these limitations, Dong and Kang [28] introduced the Global Least Squares (GLS) interpolation. As it is shown by [29], it presents a more stable behavior in the presence of strong anisotropy and highly heterogeneous media while still observing the LPC.

In the present work, we propose an extension of the MsCV by [14] to 3-D geometries coupled with the 3-D MPFA-D from [27] and the robust GLS interpolation introduced by [28]. In order to generate the multiscale geometric entities, we also extend the background grid framework proposed by [30] to 3-D geometries. Furthermore, we introduce an enhanced version of the 3-D MsCV, the E-MsCV, by incorporating the preconditioning technique from the E-MsRSB by [18] to the definition of the multiscale operators, and we employ the MsCV operators in a two-stage smoothing procedure to recover the fine-scale solution, as seen in [31,32]. We apply the developed framework to the study of the single-phase flow in anisotropic and heterogeneous porous media.

This paper is structured as follows: in Section 2, we present the mathematical formulation studied; in Section 3, we discuss the proposed numerical formulation for the fine-scale and the multiscale formulation; in Section 4, we detail the multiscale pre-processing algorithm based on the concept of a background grid; finally, in Section 5, we present some examples using the 3-D MsCV and the background grid framework.

2. Mathematical formulation

In this section, we present the mathematical model that describes the 3-D single-phase flow of an incompressible fluid in anisotropic and heterogeneous porous media. This problem can be described by the following elliptic equation:

$$\nabla \cdot \vec{\mathcal{F}} = Q(\vec{x}), \text{with } \vec{\mathcal{F}} = -\underset{\sim}{\mathcal{K}}(\vec{x})\nabla p, \tag{1}$$

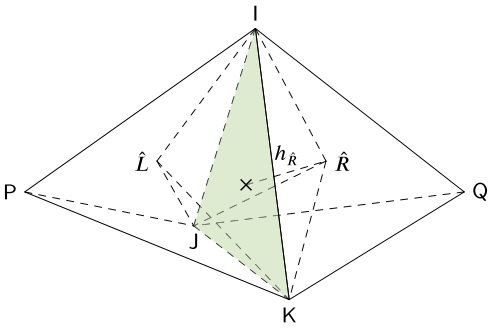

Fig. 1. Two tetrahedra $\hat{R}$ and $\hat{L}$ sharing a face IJK illustrating the main entities in the MPFA-D scheme. Adapted from [27].

where $\vec{x}$ belongs to the physical domain $\Omega \subset \mathbb{R}^3$, $\vec{\mathcal{F}}$ represents the velocity field, p is the pressure field, $\mathcal{Q}(\vec{x})$ denotes the source term, and $\underset{\sim}{\mathcal{K}}(\vec{x})$ is a positive definite symmetric full permeability tensor satisfying the ellipticity condition [33,34]. It can be expressed in Cartesian coordinates as follows:

$$\underset{\sim}{\mathcal{K}}(\vec{x}) = \begin{pmatrix} K_{xx} & K_{xy} & K_{xz} \\ K_{xy} & K_{yy} & K_{yz} \\ K_{xz} & K_{yz} & K_{zz} \end{pmatrix}. \tag{2}$$

Typical boundary conditions for Equation (1) are given by:

$$p = g_D \quad \text{for } \vec{x} \in \Gamma_D, \tag{3}$$

$$\vec{\mathcal{F}}(\vec{x}) \cdot \vec{n} = g_N \quad \text{for } \vec{x} \in \Gamma_N, \tag{4}$$

where Γ_D and Γ_N represent the Dirichlet and Neumann boundaries, respectively, with $\Gamma_D \cap \Gamma_N = \varnothing$, and $\vec{n}$ denotes the unit outward normal vector.

3. Numerical formulation

3.1. Fine-scale discretization

To discretize Equation (1) at the fine-scale, we have employed the Multipoint Flux Approximation with a Diamond stencil (MPFA-D) method, as proposed by [27], replacing the original nodal interpolation algorithm with the Global Least Squares (GLS) interpolation of the vertex unknowns, as devised by [28].

To ensure clarity, we adopt an overloaded notation and consider Ω to also represent the discrete computational domain, while Γ denotes its associated boundary. Additionally, Ω can be subdivided into a set of n_k non-overlapping control volumes. By integrating Equation (1) over an individual control volume $\hat{R}$ and applying Gauss's theorem, the following expression is obtained:

$$\int_{\Omega_{\hat{R}}} \nabla \cdot \vec{\mathcal{F}} \, \mathrm{d}\Omega_{\hat{R}} = \int_{\Gamma_{\hat{R}}} \vec{\mathcal{F}} \cdot \vec{n} \, \mathrm{d}\Gamma_{\hat{R}} = \int_{\Omega_{\hat{R}}} \mathcal{Q} \, \mathrm{d}\Omega_{\hat{R}}, \tag{5}$$

where $\Omega_{\hat{R}}$ and $\Gamma_{\hat{R}}$ denote the volume and the boundary of the control volume $\hat{R}$, respectively. By applying the mean value theorem, Equation (5) can be rewritten as:

$$\sum_{m \in \Gamma_{\hat{R}}} (\vec{\mathcal{F}} \cdot \vec{N})|_m = \overline{\mathcal{Q}}_{\hat{R}} \Omega_{\hat{R}}, \tag{6}$$

where $\overline{\mathcal{Q}}_{\hat{R}}$ is the average source term in $\hat{R}$, m is a face of $\hat{R}$ and $\vec{n}$ is the area vector associated to m. As discussed in [21,22], various strategies can be employed to approximate the flux expression described in Equation (6), leading to the development of different schemes.

3.1.1. The Multipoint Flux Approximation with a Diamond stencil (MPFA-D)

The MPFA-D belongs to the CVD-MPFA (control-volume-distributed MPFA) family of schemes for the discretization of the pressure equation on structured and unstructured grids [35], and it provides a full pressure support [36] discretization of Equation (1) for 3-D tetrahedral meshes. Other authors have already investigated different MPFA alternatives in two and three dimensions, including unstructured tetrahedral grids [35].

Given the arrangement shown in Fig. 1, the MPFA-D flux through the face IJK is approximated by:

$$\vec{\mathcal{F}}_{\hat{R}} \cdot \vec{N}_{\mathrm{IJK}} \approx -K^n_{\mathrm{eff}} \left[2(p_{\hat{R}} - p_{\hat{L}}) - D_{JI}(p_I - p_J) - D_{JK}(p_K - p_J) \right], \tag{7}$$

where K^n_{eff} is the face transmissibility written as:

$$K^n_{\text{eff}} = \frac{K^n_{\hat{R}} K^n_{\hat{L}}}{K^n_{\hat{R}} h_{\hat{L}} + K^n_{\hat{L}} h_{\hat{R}}}, \tag{8}$$

and D_{JI} and D_{JK} are the cross-diffusion terms given by:

$$D_{JI} = \frac{\overrightarrow{\tau_{JK}} \cdot \overrightarrow{\hat{L}\hat{R}}}{|\overrightarrow{N}_{\text{IJK}}|^2} - \frac{1}{|\overrightarrow{N}_{\text{IJK}}|} \left(\frac{K^{JK}_{\hat{R}}}{K^n_{\hat{R}}} h_{\hat{R}} + \frac{K^{JK}_{\hat{L}}}{K^n_{\hat{L}}} h_{\hat{L}} \right)$$

$$D_{JK} = \frac{\overrightarrow{\tau_{JI}} \cdot \overrightarrow{\hat{L}\hat{R}}}{|\overrightarrow{N}_{\text{IJK}}|^2} - \frac{1}{|\overrightarrow{N}_{\text{IJK}}|} \left(\frac{K^{JI}_{\hat{R}}}{K^n_{\hat{R}}} h_{\hat{R}} + \frac{K^{JI}_{\hat{L}}}{K^n_{\hat{L}}} h_{\hat{L}} \right),$$

with:

$$K^n_{\hat{r}} = \frac{\overrightarrow{N}^T_{\text{IJK}} \underset{\sim}{K}_{\hat{r}} \overrightarrow{N}_{\text{IJK}}}{2|\overrightarrow{N}_{\text{IJK}}|} \tag{9}$$

$$K^{ij}_{\hat{r}} = \frac{\overrightarrow{N}^T_{\text{IJK}} \underset{\sim}{K}_{\hat{r}} \overrightarrow{\tau}_{ij}}{2|\overrightarrow{N}_{\text{IJK}}|} \tag{10}$$

$$\overrightarrow{\tau}_{ij} = \overrightarrow{N}_{\text{IJK}} \times \overrightarrow{ij}, \tag{11}$$

for $i, j = I, J, K$ and $r = R, L$.

The flux on a face subjected to Dirichlet boundary conditions is given by:

$$\overrightarrow{\mathcal{F}}_{\hat{R}} \cdot \overrightarrow{N}_{\text{IJK}} \approx - \left[2 \frac{K^n_{\hat{R}}}{h_{\hat{R}}} (p_{\hat{R}} - g^D_J) + D_{JI}(g^D_J - g^D_I) + D_{JK}(g^D_J - g^D_K) \right], \tag{12}$$

where g^D_I, g^D_J and g^D_K are the prescribed pressure values on the boundary, with D_{JI} and D_{JK}:

$$D_{JI} = \frac{\left(\overrightarrow{\tau_{JK}} \cdot \overrightarrow{J\hat{R}} \right)}{|\overrightarrow{N}_{\text{IJK}}|} \frac{K^{(n)}_{\hat{R}}}{h_{\hat{R}}} + K^{JK}_{\hat{R}}, \tag{13}$$

$$D_{JK} = \frac{\left(\overrightarrow{\tau_{JI}} \cdot \overrightarrow{J\hat{R}} \right)}{|\overrightarrow{N}_{\text{IJK}}|} \frac{K^{(n)}_{\hat{R}}}{h_{\hat{R}}} + K^{JI}_{\hat{R}}. \tag{14}$$

Furthermore, for faces on the Neumann boundary, we have:

$$\overrightarrow{\mathcal{F}}_{\hat{R}} \cdot \overrightarrow{N}_{\text{IJK}} = g_N. \tag{15}$$

3.1.2. Vertex unknowns interpolation

As it can be seen from Equation (7), the MPFA-D unique flux expression, apart from the cell unknowns, includes vertex unknowns that must be eliminated in order to obtain a completely cell-centered approximation. This can be achieved by rewriting the vertex variables as a linear combination of the surrounding cell-centered values:

$$p_\upsilon = \sum_{\hat{k}=1}^{n_k} \omega_{\hat{k}} p_{\hat{k}}. \tag{16}$$

Here, we have opted to use the Global Least Squares (GLS) interpolation by [28]. It is a linear-preserving interpolation technique capable of handling heterogeneous and highly anisotropic media while maintaining a good convergence rate as discussed by [29].

Dong and Kang [28] introduce the following metric for the magnitude of the anisotropy of the permeability coefficient $\underset{\sim}{K}$:

$$\mathcal{A}(\underset{\sim}{K}) = \left(1 - \frac{3(\det \underset{\sim}{K})^{1/3}}{\operatorname{tr} \underset{\sim}{K}} \right)^2. \tag{17}$$

It allows to take into account the physical aspects of the problem in addition to the geometric ones during the calculation of the weights.

A piecewise linear function is also defined around the interpolated node υ:

$$P_i(\vec{x}) = \vec{g}^T_i (\vec{x} - \vec{x}_\upsilon) + p_\upsilon, \tag{18}$$

in which $\vec{g}_i$ are the coefficients of the linear combination and $\vec{x}_\upsilon$ is the position of the node υ.

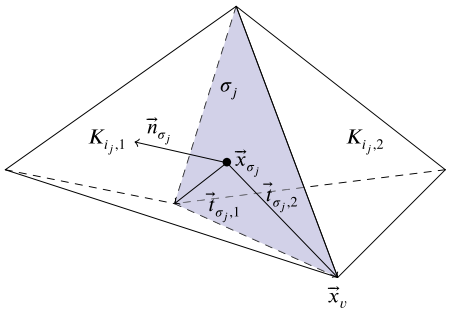

Fig. 2. Local structure and notation for an internal node. Adapted from [28].

For an internal node, as illustrated in Fig. 2, the weights of the GLS interpolation are computed by finding the least squares (LS) solution of:

$$\min_{\mathbf{V}} \left(\sum_{i=1}^{n_K} (\delta U_i)^2 + \sum_{j=1}^{n_f} \left[(\delta F_j)^2 + (\delta T_{j,1})^2 + \tau_{j,2}^2 (\delta T_{j,2})^2 \right] \right), \tag{19}$$

where n_K and n_f are the number of control volumes and the number of faces surrounding node v, respectively. Furthermore:

$$\tau_{j,2} = |\vec{t}_{\sigma_j,2}|^{-\eta_j} \tag{20}$$

$$\eta_j = \max\left(\mathcal{A}(\underset{\sim}{\mathcal{K}}_{i_{j,1}}), \mathcal{A}(\underset{\sim}{\mathcal{K}}_{i_{j,2}}) \right) \tag{21}$$

$$\begin{aligned}
\delta U_i &= P_i(\vec{x}) - p_i, \\
\delta F_j &= \vec{n}_{\sigma_j} \underset{\sim}{\mathcal{K}}_{i_{j,1}} \vec{g}_{i_{j,1}} - \vec{n}_{\sigma_j} \underset{\sim}{\mathcal{K}}_{i_{j,2}} \vec{g}_{i_{j,2}}, \\
\delta T_{j,1} &= \vec{t}^{\,T}_{\sigma_j,1} \vec{g}_{i_{j,1}} - \vec{t}^{\,T}_{\sigma_j,1} \vec{g}_{i_{j,2}}, \\
\delta T_{j,2} &= \vec{t}^{\,T}_{\sigma_j,2} \vec{g}_{i_{j,1}} - \vec{t}^{\,T}_{\sigma_j,2} \vec{g}_{i_{j,2}}, \\
\mathbf{U} &= (p_1, \ldots, p_{n_k})^T, \\
\mathbf{V} &= (\vec{g}_1^{\,T}, \ldots, \vec{g}_{n_k}^{\,T}, p_v)^T,
\end{aligned} \tag{22}$$

and $\vec{t}_{\sigma_j,1}, \vec{t}_{\sigma_j,2}$ are non co-linear tangent vectors to the face σ_j.

The problem described by Equation (19) can be rewritten in matrix form as:

$$\mathbb{M}_v \mathbf{V} = \mathbb{N}_v \mathbf{U}, \tag{23}$$

whose LS solution is:

$$\mathbf{V} = \left(\mathbb{M}_v^T \mathbb{M}_v \right)^{-1} \mathbb{M}_v^T \mathbb{N}_v \mathbf{U}. \tag{24}$$

It follows that:

$$(\omega_1, \ldots, \omega_{n_k}) = \vec{e} \left(\mathbb{M}_v^T \mathbb{M}_v \right)^{-1} \mathbb{M}_v^T \mathbb{N}_v, \tag{25}$$

where $\vec{e}$ is the last column of a $(3n_k + 1) \times (3n_k + 1)$ identity matrix, i.e., the weights correspond to the last row of $\left(\mathbb{M}_v^T \mathbb{M}_v \right)^{-1} \mathbb{M}_v^T \mathbb{N}_v$.

For nodes on the Neumann boundary, the interpolated value takes the form:

$$p_v = \sum_{\hat{k}=1}^{n_k} \omega_{\hat{k}} p_{\hat{k}} + \omega_c, \tag{26}$$

in which ω_c stands for the contribution of the Neumann boundary value to p_v.

The minimization problem seen in Equation (19) is modified to include the contribution of the boundary condition, so that the new problem to be solved in the LS sense is:

$$\min_{\mathbf{V}} \left(\sum_{i=1}^{n_K} (\delta U_i)^2 + \sum_{j=1}^{n_f} \left[(\delta F_j)^2 + (\delta T_{j,1})^2 + \tau_{j,2}^2 (\delta T_{j,2})^2 \right] + \sum_{k=1}^{n_b} \left(\delta N_k \right)^2 \right), \tag{27}$$

where:

$$\delta N_k = -\vec{n}^{\,T}_{\sigma_{k,b}} \underset{\sim}{\mathcal{K}}_{i_k} \vec{g}_{i_k} - g_N \left(\vec{x}_{\sigma_{k,b}} \right), \tag{28}$$

n_b is the number of boundary faces surrounding the node and $g_N\left(\vec{x}_{\sigma_{k,b}}\right)$ corresponds to the Neumann boundary condition value at face $\sigma_{k,b}$.

The final solution for the weights can be found similarly to the internal nodes. For a more detailed description of the assembly procedure of these local problems, see [28].

3.2. Multiscale formulation

The core idea behind every multiscale scheme is to employ the coarse scale as an auxiliary basis to approximate the solution of the fine-scale system of equations. This is achieved by using two numerical operators that, together, are capable of projecting information back and forth between these two discrete scales: the prolongation operator **P** and the restriction operator **R**. The prolongation operator stores the basis functions, that in turn, capture the influence that each coarse volume has on its corresponding support region. On the other hand, the restriction operator **R** maps the distribution of the fine-scale quantities onto the coarse-scale. In practical terms, for a problem with a fine-scale and coarse-scale containing n_f and n_c control volumes, respectively, **P** and **R** are matrices with dimensions $n_f \times n_c$ and $n_c \times n_f$.

By definition, **P** approximates the fine-scale solution **p** by extending the coarse scale solution $\mathbf{p}_c$ onto the fine-scale space as follows:

$$\mathbf{p} \cong \mathbf{p}_{ms} = \mathbf{P}\mathbf{p}_c, \tag{29}$$

where $\mathbf{p}_{ms}$ denotes the multiscale approximate solution.

Let the fine-scale discrete system of equations be:

$$\mathbf{A}\mathbf{p} = \mathbf{q}. \tag{30}$$

In order to find $\mathbf{p_c}$, we need to find a system defined on the coarse scale, similarly to Equation (30). By replacing the approximation of the exact solution of Equation (29) in (30) and premultiplying by the restriction operator, a coarse-scale system is found:

$$\mathbf{RA}\left(\mathbf{P}\mathbf{p}_c\right) = \mathbf{R}\mathbf{q} \quad \Longrightarrow \quad \mathbf{A}_c\mathbf{p}_c = \mathbf{q}_c, \tag{31}$$

where $\mathbf{A}_c = \mathbf{RAP}$ and $\mathbf{q}_c = \mathbf{Rq}$.

Multiscale methods differentiate themselves based on how the prolongation and restriction operators are defined. In this work, we extend the Multiscale Control Volume (MsCV) [14] to 3-D domains. The MsCV method uses the prolongation operator of the Multiscale Restriction-Smoothed Basis (MsRSB) proposed by [16] in combination with the MPFA-D in 2-D. The resulting framework provides a flux approximation on the fine-scale that is consistent with unstructured meshes. To adapt the MsCV to general 3-D grids, two issues need to be addressed: the use of a consistent flux approximation and the definition of an algorithm capable of generating the multiscale geometric entities on these grids. The first issue is resolved by replacing the standard 2-D MPFA-D by the 3-D MPFA-D from [27] in which we introduce the robust GLS interpolation as defined in the previous section. The latter is addressed by extending the background grid strategy presented by [30] to 3-D geometries. Furthermore, we also propose an enhanced version of the 3-D MsCV, the E-MsCV, which applies the preconditioning technique described by [18] to improve convergence.

3.2.1. Multiscale geometric entities

In this subsection, we will summarize the geometric entities employed by the MsCV and the MsRSB methods based on the concepts introduced by [14,30,16]. The algorithms used to generate these entities will be discussed in Section 4. Illustrations to the concepts presented below are provided in Fig. 3.

Fine-scale mesh (Ω_f) The fine-scale mesh is the higher resolution discretization of the physical domain. It is usually the same grid used to estimate the physical properties of the medium.

Background grid (Ω_{bg}) The background grid is an auxiliary grid used as a reference to partition the fine-scale mesh and generate the primal and dual coarse meshes. This is a concept introduced in the multiscale context by [30] for the 2-D case. Fig. 3a presents both the fine-scale and the background grid.

Primal coarse mesh (Ω_c^P) This is a lower-resolution grid obtained by agglomerating volumes from the fine-scale mesh, as it can be seen in Fig. 3b. In the original MsCV and MsRSB methods, this mesh is generated via some partitioning tool. However, in the present work we use the concept of a background grid to determine the multiscale entities. This procedure will be further detailed in Section 4.

Dual coarse mesh (Ω_c^D) The dual coarse mesh is an auxiliary grid used to enforce mass conservation on the boundaries of the primal coarse volumes and later used in the flux reconstruction algorithm to find a conservative flux field from the multiscale solution. This grid is represented in Fig. 3c by the red regions.

Primal coarse center (x^P) The primal coarse center is the fine-scale volume closest to the centroid of the corresponding primal coarse volume. [16,37] discuss different approaches to define the primal coarse center, but we have chosen to employ the aforementioned definition for the sake of simplicity.

Support region of a primal coarse volume j (I_j) The support region can be interpreted as the region of influence of a primal coarse center in the global domain. This is equivalent to:

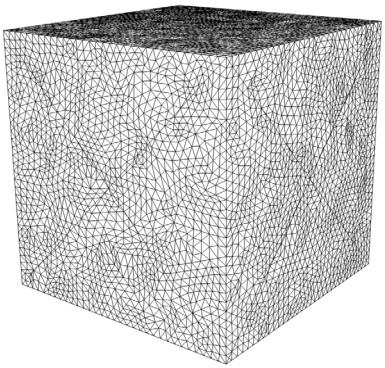

(a) The fine-scale mesh Ω_f (thin lines) and the background grid Ω_{bg} (bold lines).

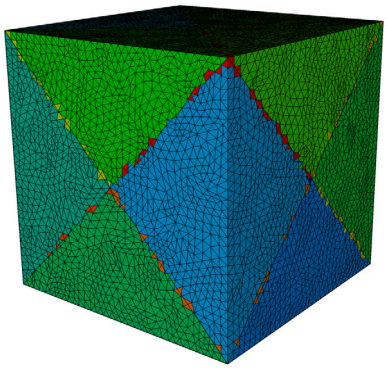

(b) The primal coarse mesh Ω_c^P.

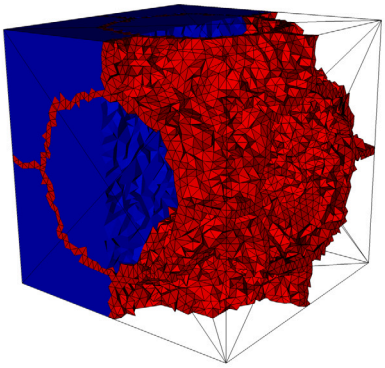

(c) The dual coarse mesh Ω_c^D (red).

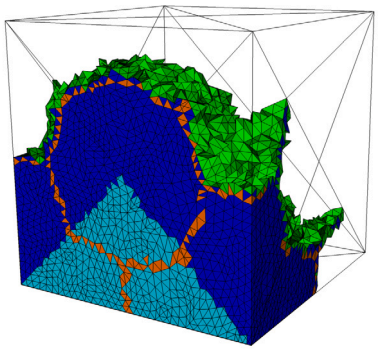

(d) An example of support region I_j (dark blue) and its boundary B_j (green) highlighting H_j (orange) and the corresponding primal volume (light blue).

Fig. 3. Illustration of the MsCV geometric entities.

$$\mathbf{P}_{i,j} \neq 0, \quad \forall i \in I_j. \tag{32}$$

It is important to note that the primal coarse center itself, as well as the support boundary B_j, is not part of the support region.

Support boundary of a primal coarse volume j (B_j) The support boundary consists of all cells that share at least one face with a cell in the support region I_j but are not a part of it themselves.

Global support boundary (G) The global support boundary is the set of all fine-scale cells that belong to the support boundary of a primal coarse volume, i.e.:

$$G = \bigcup_{j=1}^{n_c} B_j \tag{33}$$

Global support boundary in a support region (H_j) This is the set of fine-scale cells that are in the global support boundary and belong to the support region of j. Equivalently:

$$H_j = I_j \cap G \tag{34}$$

Fig. 3d illustrates an example of a support region, its boundary and the intersection with H_j.

3.2.2. The MsCV operators in 3-D

The MsCV method proposed by [14] is based on the MsRSB introduced by [16] which uses an iterative process to define the basis functions for the prolongation operator. We use the basis of the original MsCV with some adaptations for the 3-D case to define the iterative procedure of constructing the prolongation operator.

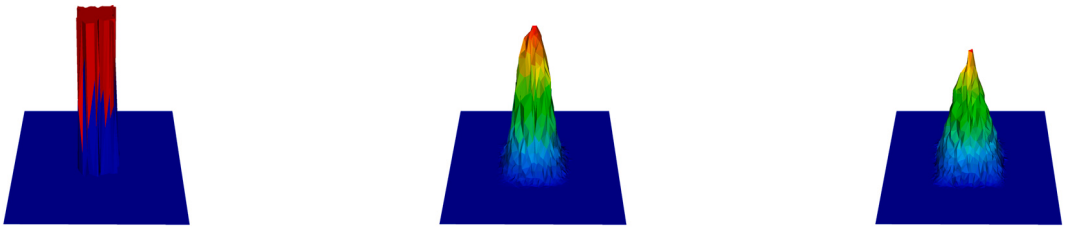

(a) Initial guess. (b) 100 iterations. (c) 500 iterations.

Fig. 4. The smoothing process of the multiscale basis functions.

The prolongation operator is initialized as the characteristic function of each primal coarse volume, i.e.,

$$P_{ij}^0 = \begin{cases} 1 & \text{if } \Omega_{f,i} \in \Omega_{c,i}^P \\ 0 & \text{otherwise} \end{cases}. \tag{35}$$

As pointed out by [16], other initial guesses could be used, but this choice is made for its simplicity and because it already provides a partition of unit. The initial operator is then modified through weighted Jacobi iterations of the form:

$$P_j^{n+1} = P_j^n - \overline{\omega} D^{-1} A^{pre} P_j^n, \tag{36}$$

where $\overline{\omega}$ is the relaxation parameter of the Jacobi iteration set to $2/3$, D^{-1} is the inverse of the main diagonal of the preconditioned MPFA-D left-hand side term, and A^{pre} is the preconditioned MPFA-D matrix. Here, the preconditioned matrix is a direct application of the technique described by [14] and is given by:

$$A_{ij}^{pre} = \begin{cases} A_{ij} & \text{if } i \neq j \\ A_{ii} - \sum_{k=1}^{n_f} A_{ik} & \text{otherwise} \end{cases}. \tag{37}$$

Given the iterative process in Equation (36), the smoothing procedure applied to compute each basis function P_j is detailed in Algorithm 1.

Algorithm 1: The MsCV iterative smoothing procedure of the basis functions.

Input: The initial guess $\mathbf{P}^0$
Output: The prolongation operator $\mathbf{P}$

1 Compute the initial increment $\hat{d}_j = -\overline{\omega} D^{-1} A^{pre} P_j^n$;

2 Modify $\hat{d}_j$ to ensure the partition of unity and avoid growth outside the support region:

$$d_{ij} = \begin{cases} \frac{\hat{d}_{ij} - P_{ij}^n \sum_{k \in H_j} \hat{d}_{ik}}{1 + \sum_{k \in H_j} \hat{d}_{ik}} & \text{if } \Omega^{f,i} \in H_j \\ \hat{d}_{ij} & \text{if } \Omega^{f,i} \in I_j \text{ and } \Omega^{f,i} \notin H_j \\ 0 & \text{otherwise} \end{cases}$$

3 Set $P_j^{n+1} = P_j^n + d_j$;
4 Set $P_{i,j}^{n+1} = 1$ for all fine-scale cells i that belong solely to the support region of the primal center j;
5 Rescale P_j to ensure partition of unity, i.e., set $P_j^{n+1} = P_j^{n+1} / \sum_i P_{i,j}$;
6 Calculate the local error for cells outside the global support boundary:

$$e_j = \max_{i \notin G} |d_{ij}|$$

7 If $\|\mathbf{e}\|_\infty \leq tol$, stop and set $P = P^{n+1}$. Else, go to step 1;

Fig. 4 illustrates the smoothing procedure of the basis functions. The 4^{th} step of the procedure is performed in order to ensure mass conservation since the fine-scale cells involved in this calculation contribute only to the support region of the coarse cell j and, therefore, should hold the maximum value in the prolongation operator.

Finally, for the restriction operator, we use the Finite Volume restriction operator from [6] defined as:

$$\mathbf{R}_{ij} = \begin{cases} 1 & \text{if } \Omega^{f,j} \in \Omega_{c,i}^P \\ 0 & \text{otherwise} \end{cases}. \tag{38}$$

3.2.3. The enhanced MsCV (E-MsCV)

As discussed by [18], the MsRSB prolongation operator may show slow convergence when applied to non M-matrices. To overcome this issue, a modification to the fine-scale matrix is suggested so that the M-matrix properties are reinforced, making the convergence rate of the method closer to when it is applied to a TPFA matrix.

As we will show in our experiments, the 3-D MsCV presents the same convergence issues. Since the MsCV prolongation operator is based on the MsRSB, it is natural to consider the application of the aforementioned procedure to our new framework. We designate this modified version of the MsCV the *Enhanced MsCV* (E-MsCV).

The E-MsCV improves on the MsCV by adopting the preconditioning technique from [18]. It modifies the transmissibility matrix A by filtering all positive off-diagonal entries. This ensures M-matrix properties and improves the convergence rate of the Jacobi iterations. This preconditioning technique can be written as:

$$A^*_{ij} = \min\left(A_{ij}, 0\right), \tag{39}$$

$$A^{pre}_{ij} = \begin{cases} A^*_{ij} & \text{if } i \neq j \\ A^*_{ii} - \sum_{k=1}^{n_f} A^*_{ik} & \text{otherwise} \end{cases}. \tag{40}$$

The remaining of the E-MsCV follows the same iterative procedure described in Algorithm 1.

3.2.4. The MsCV iterative procedure

Although the multiscale solution could be used as a good approximation of the fine-scale solution, in some cases, e.g. on highly heterogeneous media, it may not completely capture the underlying phenomena. It would be desirable to correct the multiscale solution so it is closer to the reference solution. Zhou and Tchelepi [9] proposed an iterative correction of the prolongation operator in the context of the simulation of compressible flow in porous media. Meanwhile, the i-MSFV (Iterative MsFV) [31] incorporates the idea of an iterative correction of the basis functions to a sequence of line relaxation smoothing steps of the multiscale solution, borrowed from multigrid methods, here still applied to Cartesian grids. Lunati et al. [32] recast the MsFV into a two-stage iterative method that is then employed within the GMRES iterations. Analogously, a two-stage approach was also applied in a Richardson type iteration in [10,38]. Furthermore, a two-stage iterative procedure was also described for the MsRSB in [16].

In this work, we employ the procedure described in [30,32], which consists in a two-stage smoother. First, the multiscale operators are used to compute a pressure increment using the coarse-scale matrix. Then, an additional smoothing step is applied to obtain the new solution. In our implementation, the smoothing stage described in line 7 of Algorithm 2 is achieved using either the Biconjugate Gradient Stabilized method (BiCGSTAB) or the Generalized Minimal Residual method (GMRES) [39], the choice depending on the problem, and an ILU(0) preconditioner.

Algorithm 2: The MsCV iterative smoothing procedure of the basis functions.

Input: The fine-scale LHS $\mathbf{A}$, the fine-scale RHS $\mathbf{q}$, the prolongation operator $\mathbf{P}$ and the restriction operator R.
Output: The iterative solution, $\mathbf{p}_{it}$

1 $\mathbf{p}^{(n)} \leftarrow \mathbf{p}_{ms}$; ▷ *The initial guess for the iterative procedure.*
2 $\mathbf{r}^{(n)} \leftarrow \mathbf{q} - \mathbf{A}\mathbf{p}^{(n)}$; ▷ *The initial residual vector.*
3 $\mathbf{A}_c \leftarrow \mathbf{RAP}$; ▷ *The coarse scale matrix.*
4 **while** $||\mathbf{r}^{(n)}||_2 > \varepsilon$ **do**
5 $\quad \delta\mathbf{p}^{(n+1/2)}_{ms} \leftarrow (\mathbf{P}\mathbf{A}_c^{-1}\mathbf{R})\mathbf{r}^{(n)}$; ▷ *Compute the increment given by the multiscale approximation.*
6 $\quad \mathbf{r}^{(n+1/2)} \leftarrow \mathbf{r}^{(n)} - \mathbf{A}\delta\mathbf{p}^{(n+1/2)}_{ms}$;
7 $\quad \delta\mathbf{p}^{(n+1/2)} \leftarrow \mathbf{A}^{-1}\mathbf{r}^{(n+1/2)}$; ▷ *Smoothing stage.*
8 $\quad \mathbf{p}^{(n+1)} \leftarrow \mathbf{p}^{(n)} + \delta\mathbf{p}^{(n+1/2)}_{ms} + \delta\mathbf{p}^{(n+1/2)}$; ▷ *Update the solution.*
9 $\quad \mathbf{r}^{(n+1)} \leftarrow \mathbf{q} - \mathbf{A}\mathbf{p}^{(n+1)}$; ▷ *Update the residual.*
10 $\quad n \leftarrow n + 1$;
11 **end**
12 $\mathbf{p}_{it} \leftarrow \mathbf{p}^n$;

3.2.5. Flux reconstruction algorithm

By construction, the multiscale solution is mass conservative on the coarse scale. However, if the prolonged solution is used to calculate the fluxes on the fine scale, the resulting field will not be mass conservative since the algorithm used to obtain the prolongation operator decouples the domain for the solution of local problems within each support region. Hence, one must compute a new pressure field to accommodate the error introduced by the initial multiscale solution while keeping the mass conservation on the interfaces of the primal coarse cells. In this work, a procedure based on [6] and [14] is employed to obtain such pressure field.

The reconstructed pressure field is composed by the original multiscale solution on the boundaries of the primal coarse volume and a new solution computed in the interior of the coarse cell. First, we determine the fluxes on the surface of each primal coarse cell using the prolonged solution. Next, for each coarse cell, we use the fluxes calculated on the previous step as Neumann boundary conditions to solve Equation (1) restricted to the primal coarse volume. This can be written as:

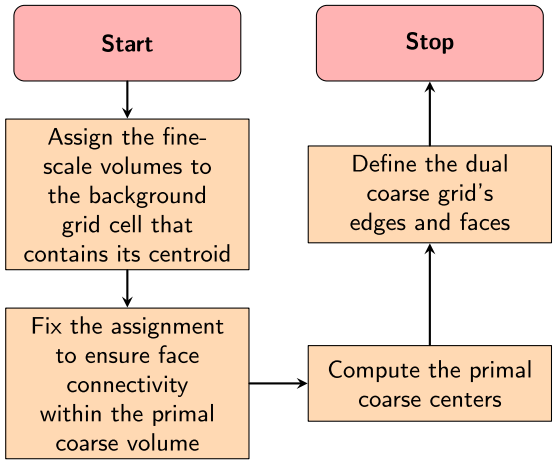

Fig. 5. Main steps of the background grid framework for 3-D geometries.

$$\begin{cases} -\nabla \cdot \left(\underset{\sim}{\mathcal{K}} \nabla \overline{p}\right) = q_f & \text{in } \Omega^P, \\ \nabla \overline{p} \cdot \vec{n} = v^{ms} & \text{on } \partial\Omega^P, \\ \overline{p} = p_{ms} & \text{in } x^P \text{ if } \partial\Omega^P \cap \Gamma_D = \varnothing \end{cases}, \tag{41}$$

where $\overline{p}$ is the new pressure field computed inside each primal coarse cell, $\vec{n}$ is the outward normal unit vector to the interface, p_{ms} is the initial multiscale solution obtained by the prolongation of the coarse scale solution and v^{ms} is the flux field computed using p_{ms}. The latter condition on Equation (41) ensures that each local problem is well posed even for the primal coarse volumes that do not contain any volumes on the fine-scale lying on the Dirichlet boundary by forcing the primal coarse center to hold its initial value.

4. Multiscale pre-processing algorithm based on a background grid

One of the key phases of any variant of the MsFV framework is the generation of the primal and dual coarse grids. Properly defining these meshes can substantially reduce the number of steps taken by the iterative multiscale procedure.

A common approach to generate the primal coarse grid is by subdividing the computational domain using a partitioning tool such as Metis [40]. That is the alternative adopted by [14,16,41]. Although straightforward, this procedure has the shortcoming of often being solely based on the geometry of the domain which in turn may lead to inconsistencies and loss of accuracy on the solution in the presence of highly heterogeneous media, as pointed out by [16,42,43], who resort to mesh adaptation to mitigate these issues.

Souza et al. [30] introduce a new procedure to generate the multiscale coarse grids by employing an auxiliary *background grid* that guides the definition of both the primal and dual coarse meshes. The background grid scheme is designed based on three assumptions:

1. The fine-scale grid is derived from the geological discretization of the domain;
2. The primal coarse grid should conform to the geological features of the medium; and
3. As far as possible, the grids from the background grid framework should be applicable to the upscaling context. Hence, strongly non-convex volumes should be avoided.

In this work, we propose a non-trivial 3-D extension of the original 2-D background grid framework and apply it to generate the multiscale coarse grids used for the simulations. The main steps of the algorithm are outlined in the flowchart in Fig. 5. We point out that the advantages of employing a background grid are twofold: first, it can be adapted to any features of interest present in the media, resulting in basis functions that better represent the heterogeneities in the reservoir; second, the background grid is used as a proxy for the coarse-scale entities, avoiding the need to deal with average properties and irregularities that may arise in a typical geometry-based partition process as in [44,40].

First, the fine-scale volumes are assigned to the background grid cell that contains its centroid in order to obtain an initial partition of the domain. This idea is equivalent to the cookie-cutter approach described in [44]. Next, the assignment is adjusted so that each partition is formed by fine-scale volumes sharing at least one face. After that, the primal coarse centers are computed by choosing the nearest fine-scale volume in the primal coarse cell to the corresponding background grid volume. Once the primal coarse grid is fully defined, we can generate the coarse dual grid. Finally, the support regions for each primal coarse center are delimited. The described steps are detailed in the Algorithms 3, 4 and 5.

5. Numerical results

In this section, we present a series of examples to evaluate the performance of the proposed 3-D MsCV and E-MsCV. In the first test, we have manufactured a simple problem with a 1-D linear solution in a conical domain in order to evaluate the performance of

Algorithm 3: Primal coarse grid generation.

Input: The fine-scale grid and the background grid
Output: The primal coarse grid
Assign each fine-scale volume to the background grid volume that contains its centroid;
For each agglomerate of fine-scale volumes, construct a graph of face connectivity within the set, i.e., an edge in the graph represents that a face is shared between two volumes;
$S \leftarrow$ a linked list containing the fine-scale volumes in disconnected components of the graphs from the previous step;
while *S is not empty* **do**
  Get the first volume from S;
  if *the volume is connected to a well formed primal coarse volume* **then**
    Assign the volume to this primal volume;
  else
    Push the volume to end of S;
  end
end

Algorithm 4: Dual coarse grid generation.

Input: The fine-scale grid, the primal coarse grid and the background grid
Output: The dual coarse grid
for *each primal coarse volume* **do**
  Determine the line segments connecting the primal volume center to its faces centers;
  Find the fine-scale volumes intercepted by the line segments and set them as coarse dual edges;
  Form the pairs of primal coarse faces sharing an edge;
  for *each pair of primal faces* **do**
    Define the plane section formed by the faces' centers and the primal coarse center;
    Find the fine-scale volume in the primal coarse volume that are intercepted by the plane section;
    Set the fine-scale volumes from the previous step as coarse dual faces;
  end
end

Algorithm 5: Support regions definition.

Input: The fine-scale grid, the primal coarse grid, the dual coarse grid and the background grid
Output: The support region of each primal coarse center
for *each primal coarse volume* C_j **do**
  Find the primal volumes sharing at least a node by using the background grid;
  Retrieve the dual faces that intercept the node neighbors;
  Define B_j as the surface surrounding the primal coarse volume using the dual faces found in the previous step;
  Set $I_j \leftarrow C_j$ as the initial support region;
  while *there are fine-scale volumes to be incorporated to the support region* **do**
    $I_j^+ \leftarrow$ the fine-scale volumes that share at least a face with a fine-scale volume in I_j;
    if $I_j^+ - I_j - B_j \neq \emptyset$ **then**
      $I_j \leftarrow I_j \cup (I_j^+ - B_j)$;
    else
      Stop;
    end
  end
end

the 3-D MsCV using a homogeneous and isotropic medium and showcase the ability of the background grid framework to generate the multiscale grids on unconventional geometries. The second example was adapted from [45] in a homogeneous and mildly anisotropic medium. In the third example, we consider a heterogeneous and strongly anisotropic medium with a constant source term. In the last example, we study a reservoir with a spherical fault and discuss the multiscale solutions on a barrier and a channel configuration.

For all examples, we have performed the simulations employing the 3-D MsCV and the E-MsCV. All the results are also compared with the standard MsRSB with a TPFA fine-scale discretization as described by [16]. Furthermore, we also show the application of the MsCV iterative procedure presented in Section 3.2.4 using the E-MsCV operators in all studied scenarios.

As in [14], we define the following error norms for the multiscale solution:

$$||\mathbf{p}^{ref} - \mathbf{p}^{ms}||_2 = \left(\frac{\sum_{\Omega_i \in \Omega_f} |p_i^{ref} - p_i^{ms}|^2}{\sum_{\Omega_i \in \Omega_f} |p_i^{ref}|^2} \right)^{1/2}, \tag{42}$$

$$||\mathbf{p}^{ref} - \mathbf{p}^{ms}||_\infty = \frac{\max_{\Omega_i \in \Omega_f} |p_i^{ref} - p_i^{ms}|}{\max_{\Omega_i \in \Omega_f} |p_i^{ref}|}, \tag{43}$$

(a) Primal coarse grid. (b) Dual coarse grid (red).

Fig. 6. The multiscale coarse grids used for the simulation in the cone-shaped domain.

Table 1
The L_2 and L_∞ norms of the errors for the homogeneous and isotropic medium in a cone-shaped domain case.

Error (%)	MsCV	E-MsCV	Iterative E-MsCV	MsRSB	Iterative MsRSB
$\|\|u\|\|_2$	0.11	0.14	2×10^{-9}	0.11	4×10^{-10}
$\|\|u\|\|_\infty$	7.73	7.00	1×10^{-3}	6.57	3×10^{-4}

where the superscripts *ms* and *ref* correspond to the multiscale solution and the reference fine-scale solution, respectively.

5.1. Homogeneous and isotropic medium in a cone-shaped domain

In the first example, we study the simulation of the single-phase incompressible flow in a homogeneous and isotropic medium. The domain has the shape of a cone around the Cartesian z-axis with height and radius equal to 1 and 3, respectively. We consider the following exact solution:

$$u(x,y,z) = z, \tag{44}$$

with permeability tensor given by:

$$\underset{\sim}{K}(x,y,z) = \begin{pmatrix} 1 & 0 & 0 \\ 0 & 1 & 0 \\ 0 & 0 & 1 \end{pmatrix}. \tag{45}$$

For all problems solved here, Dirichlet boundary conditions are applied to the whole domain boundary.

For this simulation, we have used a fine-scale grid containing 119,840 cells and an unstructured background grid with 272 tetrahedra. In Fig. 6, the multiscale coarse grids used for the simulation are shown. The background grid based pre-processing framework is capable of generating coherent unstructured grids suited for simulation even for unconventionally shaped domains, as it is the case.

Table 1 presents the L_2 and L_∞ norms of the error calculated for the multiscale solutions. For the MsRSB solution, the error is computed relative to the TPFA fine-scale solution since it is as accurate as the MPFA-D. The MsCV and E-MsCV have similar performances and are as accurate as the MsRSB, the L_2 norm of the error lower than 0.2% while the L_∞ norm sits around 7%. This can also be seen in Fig. 7. All three solutions are qualitatively very close. However, by applying a single step of the MsCV iterative procedure, the error on the E-MsCV solution is reduced to near zero.

We have also applied the iterative procedure using the MsRSB operators computed with the TPFA system. The MPFA-D solution is also recovered when this combination is employed, as seen in Table 1. As discussed in [38], but also a known result in the context of domain decomposition methods [46,47], the main purpose of the multiscale stage is to provide a global problem that couples each of the local subproblems. Therefore, although desirable and potentially helpful, the accuracy of the coarse-scale solution is not the main concern. Instead, it is sufficient that the basis functions capture the main features of the underlying problem.

Although the multiscale solutions are comparable regarding their accuracy, there are notorious differences in the convergence of the basis functions. For a prescribed residual tolerance of 10^{-3}, the E-MsCV requires 276 iterations to converge, while the MsRSB takes 182 iterations. On the other hand, the original formulation of the MsCV had to be halted after 500 iterations to achieve the same level of accuracy.

5.2. Homogeneous and mildly anisotropic case

For this example, we consider the Test Case 1 proposed by [45] with a regular solution over the domain $\Omega = [0,1]^3$ given by (46) and implying in a non-homogeneous Dirichlet condition over the whole domain boundary Γ:

$$u(x,y,z) = 1 + \sin(\pi x)\sin\left(\pi\left(y+\frac{1}{2}\right)\right)\sin\left(\pi\left(z+\frac{1}{3}\right)\right), \tag{46}$$

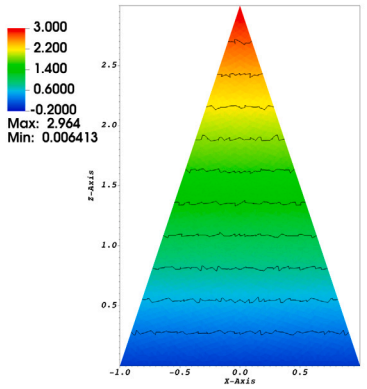

(a) Fine-scale solution.

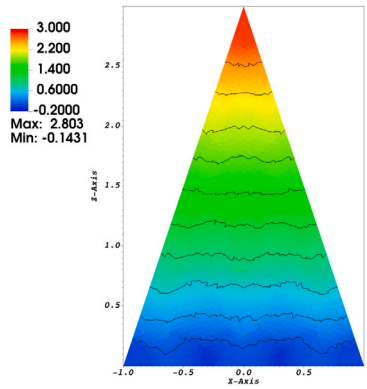

(b) MsCV solution.

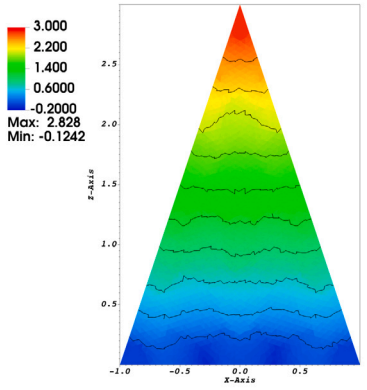

(c) E-MsCV solution.

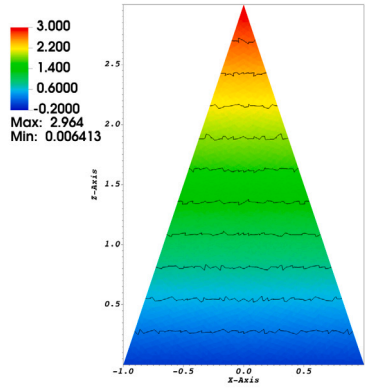

(d) Iterative E-MsCV solution.

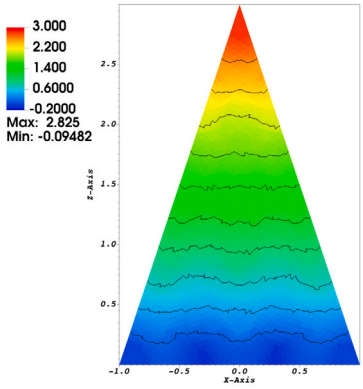

(e) MsRSB solution.

Fig. 7. The fine-scale reference solution (a) and the multiscale solutions using the MsCV (b), the E-MsCV (c), the iterative E-MsCV procedure (d) and the MsRSB (e) techniques. Slice at $y = 0$ highlighting the contour lines.

and an anisotropic permeability tensor given by:

$$\underset{\sim}{\mathcal{K}}(x, y, z) = \begin{pmatrix} 1 & 0.5 & 0 \\ 0.5 & 1 & 0.5 \\ 0 & 0.5 & 1 \end{pmatrix}. \tag{47}$$

We have executed the simulations on a fine-scale grid containing 243,840 tetrahedral cells and, to compute the multiscale solutions, we have used a prismatic background grid containing 256 cells, which corresponds to a coarsening ratio of around 952, and an unstructured tetrahedral background grid with 192 cells, with a coarsening ratio of around 1,270. For each grid, we have performed simulations with the MsCV, the E-MsCV and the MsRSB.

Table 2
The L_2 and L_∞ norms of the errors for the homogeneous and mildly anisotropic case on a prismatic background grid.

Error (%)	MsCV	E-MsCV	Iterative E-MsCV	MsRSB	Iterative MsRSB
$\|\|u\|\|_2$	0.44	0.24	1×10^{-8}	0.27	3×10^{-9}
$\|\|u\|\|_\infty$	16.45	12.07	2×10^{-3}	13.24	8×10^{-4}

Table 3
The L_2 and L_∞ norms of the errors for the homogeneous and mildly anisotropic case on a tetrahedral background grid.

Error (%)	MsCV	E-MsCV	Iterative E-MsCV	MsRSB	Iterative MsRSB
$\|\|u\|\|_2$	0.40	0.28	5×10^{-8}	0.24	8×10^{-8}
$\|\|u\|\|_\infty$	16.12	14.97	7×10^{-3}	16.63	4×10^{-3}

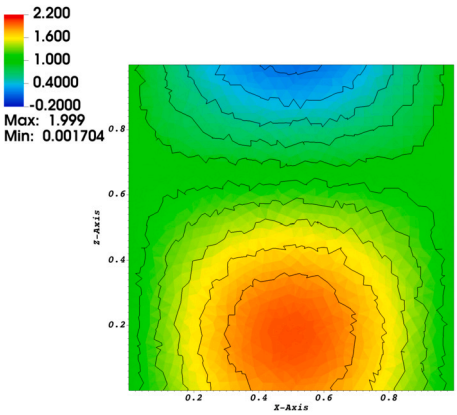

Fig. 8. The fine-scale MPFA-D solution for the homogeneous and mildy anisotropic case. Slice at $y = 0$.

In the Tables 2 and 3, the L_2 and L_∞ norms of the error from each execution are presented. In all scenarios for multiscale solutions, the L_2 norm of the error is less than 0.5% with a reasonable but significant error on the L_∞ norm. The MsCV and E-MsCV perform as well as the MsRSB despite the introduction of anisotropy which is expected since the anisotropy ratio in the problem is low and the TPFA, despite inconsistent, can still provide good solutions in this kind of scenario. Furthermore, by applying the iterative procedure described in Section 3.2.4 to the E-MsCV solution, the error can be virtually nullified in a single iteration. Similarly, the MPFA-D reference solution can also be recovered using the MsRSB operators in the multiscale stage of the iterative procedure.

As it can be seen in Figs. 9 and 10, the solutions are relatively close to the reference solution in Fig. 8, specially the solution computed on a prismatic grid. Although the multiscale approximations on a tetrahedral coarse grid yield some unphysical “fingers” in the pressure field, overall, the main aspects of the fine-scale reference are captured.

In this example, the multiscale solutions on a prismatic background grid produce lower errors than their tetrahedral counterparts. This is partially justified by the fact that, in a homogeneous medium, the support regions generated in the prismatic background grid are more compact and produce basis functions that can transition more smoothly between them. In a tetrahedral background grid, on the other hand, the coarse cells may be unaligned to the solution and the permeability tensor, affecting the shape of the basis functions and, by extension, the final solution. In both cases, the smoothing procedure is capable of recovering the original solution in a single iteration.

Regarding the convergence rate of the iterative procedure used to compute the basis functions, the E-MsCV performs slightly better than the MsRSB, requiring 130 and 166 iterations to converge on the structured and unstructured scenarios, respectively, while the MsRSB takes 146 and 184 iterations in the same situations. As with the first example, the original MsCV formulation did not converge according to the tolerance criterion and was stopped after 250 iterations in both simulations. Furthermore, the latter presented some oscillatory behavior during the iterations, which was not observed in the E-MsCV and the MsRSB. Finally, in Fig. 11, the evolution of the L_2 norm of the error of the MsCV, E-MsCV and MsRSB solutions is presented as a structured hexahedral coarse-scale grid is uniformly refined. It demonstrates that both the MsCV and the E-MsCV tend to converge to the fine-scale solution as the coarse-scale grid is refined, showing a desirable consistent behavior for the multiscale solution. Furthermore, from this experiment, the MsRSB does not appear to converge to the reference solution, as it retains the errors from the TPFA system used to compute the basis functions.

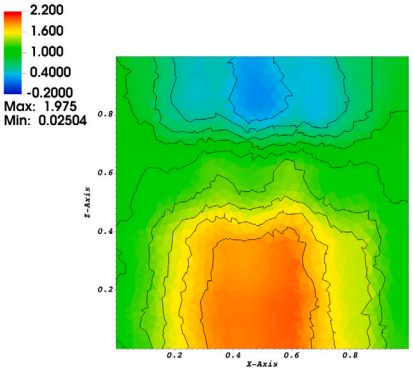

(a) MsCV solution.

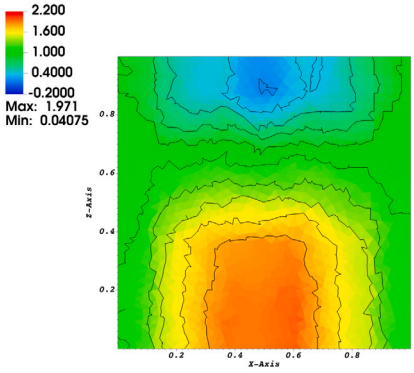

(b) E-MsCV solution.

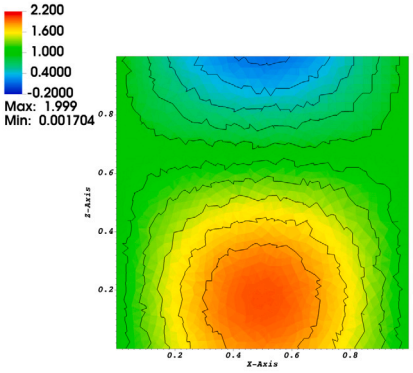

(c) Iterative E-MsCV solution.

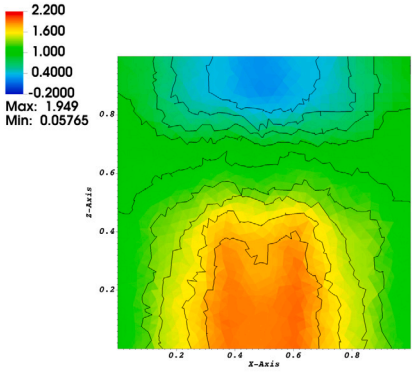

(d) MsRSB solution.

Fig. 9. The multiscale solutions on a prismatic background grid for the homogeneous and mildly anisotropic case highlighting the contour curves. Slice at $y = 0$.

5.3. Heterogeneous and strongly anisotropic case

In this example, we consider an adaptation of the third example from [30] to study the robustness of the MsCV in a heterogeneous and anisotropic medium. The problem consists in the simulation of a single-phase flow in a unitary cubic domain $\Omega = [0, 1]^3$ with the following source term:

$$Q(\vec{x}) = \begin{cases} 1, & \vec{x} \in \left[\frac{3}{8}, \frac{5}{8}\right]^3, \\ 0, & \text{otherwise} \end{cases} . \tag{48}$$

At the boundary, the Dirichlet condition $g_D = 0$ is adopted. Furthermore, the permeability tensor is the same proposed by [48] in the Case 4, illustrated in Fig. 12, and is given by:

$$\underset{\sim}{K}(x, y, z) = \frac{1}{x^2 + y^2} \begin{pmatrix} \epsilon_x x^2 + \epsilon_y y^2 & (\epsilon_x - \epsilon_y)xy & 0 \\ (\epsilon_x - \epsilon_y)xy & \epsilon_y x^2 + \epsilon_x y^2 & 0 \\ 0 & 0 & \epsilon_z(z+1)(x^2+y^2) \end{pmatrix}, \tag{49}$$

for $\epsilon_x = 1$, $\epsilon_y = 10^{-3}$ and $\epsilon_z = 10$. The simulations were conducted in a fine-scale grid with 90,831 tetrahedral cells, and the multiscale solutions were computed using a structured $5 \times 5 \times 5$ background grid and an unstructured background grid containing 96 tetrahedra adapted to the source term region. The fine-scale solution is shown in Fig. 13 and the background grid configurations can be seen in Fig. 14.

In the Tables 4 and 5, the L_2 and L_∞ norms of the error are displayed. The prolonged solutions on a structured coarse grid present a lower error on the L_2 norm, but are more susceptible to spurious oscillations since the dual edges cross the source term region, resulting in a higher L_∞ norm of the error, as it can be seen in Fig. 15. On the other hand, the solution on an unstructured grid presents a higher error on the L_2 norm but a lower and localized error on the L_∞ when compared to its structured counterpart. The adapted grid helps to reduce the spurious oscillations, but the less compact support regions tend to exacerbate the effect of the

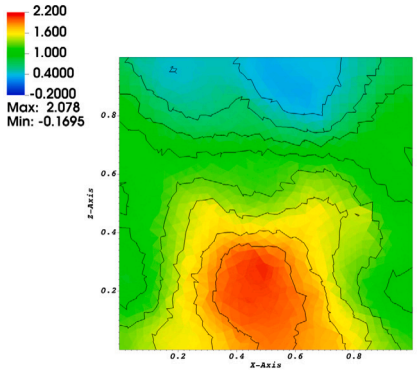

(a) MsCV solution.

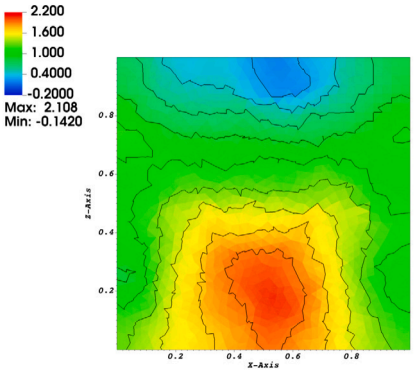

(b) E-MsCV solution.

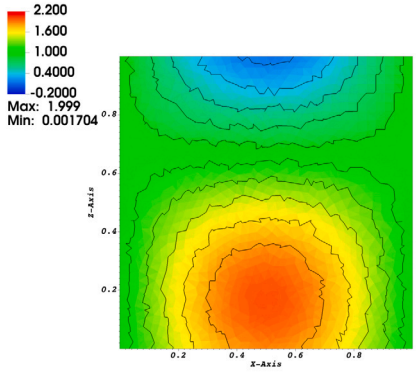

(c) Iterative E-MsCV solution.

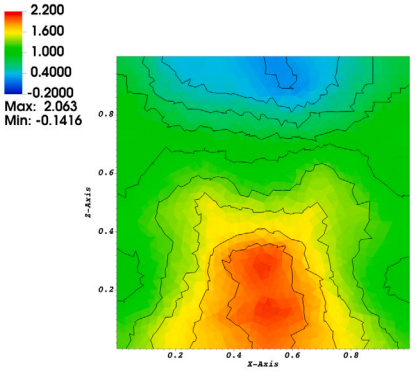

(d) MsRSB solution.

Fig. 10. Multiscale solutions on a tetrahedral background grid for the homogeneous and mildly anisotropic case highlighting the contour curves. Slice at $y = 0$.

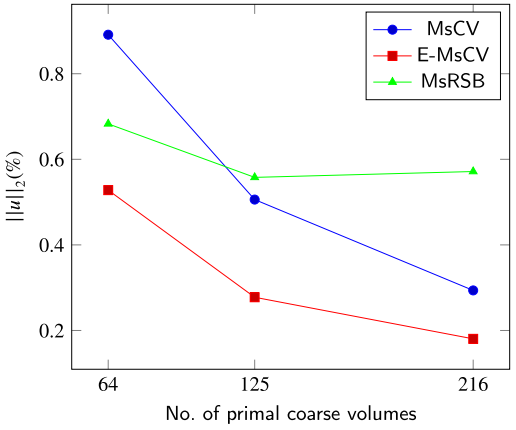

Fig. 11. Convergence rates of the multiscale solutions for the homogeneous and mildly anisotropic case.

shape of the underlying primal coarse grid, as seen in Fig. 16. Surely, the primal coarse grid could be improved or, with further developments, automatically adapted.

For this case, the relative error of the MsRSB solution was computed using the MPFA-D as the reference solution, since the TPFA solution is not consistent with the proposed problem. Comparing the MsCV and E-MsCV solutions with the MsRSB, we can notice that the errors on the L_2 norm are of the same magnitude, even though the MsRSB seems less prone to oscillations, as it is visible in Figs. 15d and 16d, and from the L_∞ norm of the error. Furthermore, by the discrete maximum principle (DMP), since the boundary conditions are non-negative, the numerical solution should also be non-negative.

Table 4
The L_2 and L_∞ norms of the errors for the heterogeneous and strongly anisotropic case on a structured background grid.

Error (%)	MsCV	E-MsCV	Iterative E-MsCV	MsRSB	Iterative MsRSB
$\|\|u\|\|_2$	18.41	4.74×10^2	3×10^{-14}	21.22	3×10^{-14}
$\|\|u\|\|_\infty$	1.3×10^4	9.5×10^4	3×10^{-4}	41.84	1×10^{-6}

Table 5
The L_2 and L_∞ norms of the errors for the heterogeneous and strongly anisotropic case on a unstructured background grid.

Error (%)	MsCV	E-MsCV	Iterative E-MsCV	MsRSB	Iterative MsRSB
$\|\|u\|\|_2$	78.90	58.32	3×10^{-14}	62.16	3×10^{-14}
$\|\|u\|\|_\infty$	83.80	69.87	3×10^{-4}	71.77	1×10^{-6}

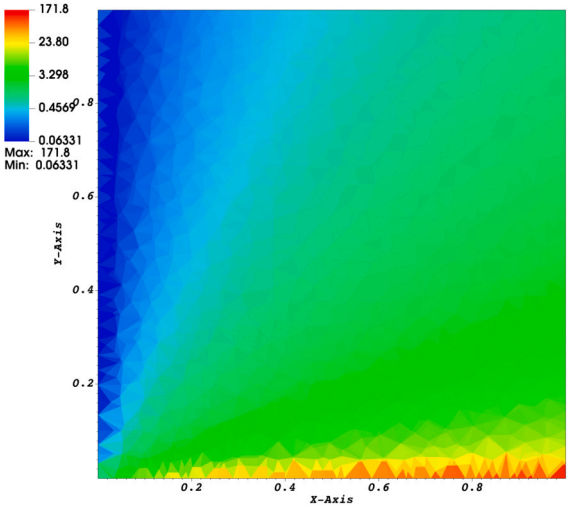

Fig. 12. Visualization of the permeability ratio $\log\left(k_{xx}/k_{xy}\right)$ of the heterogeneous and anisotropic case. Slice at $z = 0.5$.

Finally, despite the fact that the prolonged MsCV and E-MsCV solutions have a high error, the iterative procedure is still able to recover the MPFA-D fine-scale solution with great accuracy. For a residual tolerance of 10^{-4}, it takes two iterations of the procedure to obtain a solution with an error of order 10^{-14} on the L_2 norm, and 10^{-4} on the L_∞ norm for both the structured and the unstructured coarse grids, showing that the application of the MsCV operators in an iterative framework can yield good results. As in the previous examples, we were also able to recover the MPFA-D reference solution to a similar degree of accuracy using the MsRSB operators, as seen in Tables 4 and 5.

5.4. Reservoir with a spherical fault

In this final example, we study the simulation of a single-phase flow in a reservoir with a spherical barrier or channel within the domain $\Omega = [-2, 2]^3$. The following boundary conditions are applied:

$$\begin{cases} g_D = 0 & \text{on } \Gamma_{D,1} \\ g_D = 1 & \text{on } \Gamma_{D,2} \\ g_N = 0 & \text{on } \Gamma_N \end{cases}, \tag{50}$$

where $\Gamma_{D,1}$ corresponds to the planes $x = -2$, $\Gamma_{D,2}$ corresponds to the plane $x = 2$, and Γ_N is set at the planes $y = -2$, $y = 2$, $z = -2$ and $z = 2$.

The permeability field is illustrated in Fig. 17, where the fault region shaped as a sphere centered at the origin with a radius equal to 0.75 is embedded in a homogeneous domain with a permeability tensor given by:

$$\underset{\sim}{K}_1(x, y, z) = \begin{pmatrix} 1 & 0 & 0 \\ 0 & 1 & 0 \\ 0 & 0 & 1 \end{pmatrix}. \tag{51}$$

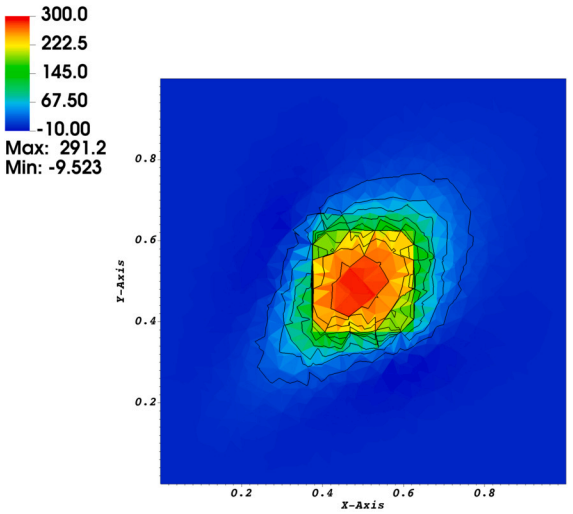

Fig. 13. The fine-scale MPFA-D reference solution for the heterogeneous and strongly anisotropic case. Slice at $z = 0.5$.

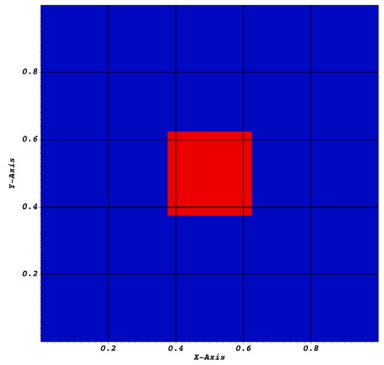

(a) Structured $5 \times 5 \times 5$ background grid.

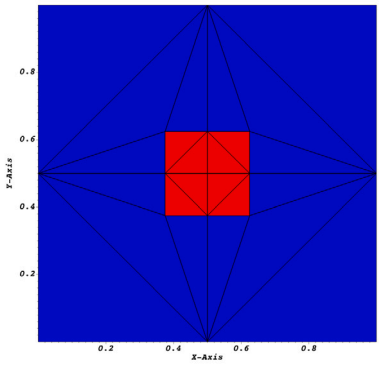

(b) Unstructured background grid.

Fig. 14. Background grids used to generate the multiscale geometric entities for the heterogeneous and strongly anisotropic case highlighting the source term region (red). Slice at $z = 0.5$.

The goal of this example is to test the changes in the solution when applying background grids that are conforming or not to the fault, and to evaluate the ability of the 3-D MsCV framework to capture such a formation. We simulate two configurations, a barrier and a channel, with permeability tensors respectively given by:

$$\underset{\sim}{\mathcal{K}}_2(x,y,z) = \begin{pmatrix} 10^{-3} & 0 & 0 \\ 0 & 10^{-3} & 0 \\ 0 & 0 & 10^{-3} \end{pmatrix} \text{ or} \tag{52}$$

$$\underset{\sim}{\mathcal{K}}_3(x,y,z) = \begin{pmatrix} 10^{3} & 0 & 0 \\ 0 & 10^{3} & 0 \\ 0 & 0 & 10^{3} \end{pmatrix}. \tag{53}$$

The simulations were conducted in a fine-scale grid with 159,893 tetrahedral cells. The fine-scale reference solutions under both configurations are presented at Fig. 18. Furthermore, the errors computed for the MsRSB solution are relative to the MPFA-D solution in this example.

In Figs. 19 and 20, the multiscale solutions for a channel configuration are shown for a structured and an unstructured background grid, respectively. In both scenarios, the MsCV and the E-MsCV are able to recover the main features of the fine-scale solution and correctly depict the influence of the channel region in the pressure field. The unstructured version is, however, prone to oscillations near the boundary as a consequence of some primal coarse volumes sharing only an edge or a node on the boundary leading to basis functions whose influence is not well spread into the boundary. Furthermore, when compared to the MsRSB, the MsCV and E-MsCV provide qualitatively close solutions. These observations are corroborated by the errors shown in Tables 6 and 7, as both norms of the error for the MsCV, E-MsCV and MsRSB are all with the same magnitude.

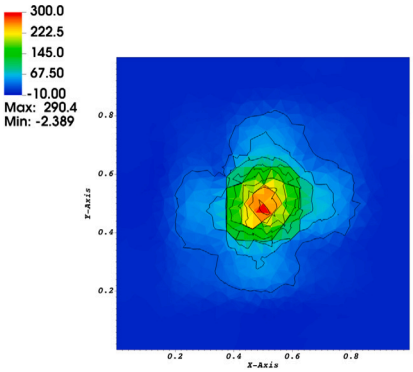

(a) MsCV solution.

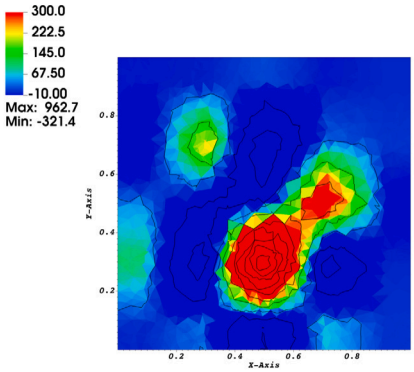

(b) E-MsCV solution.

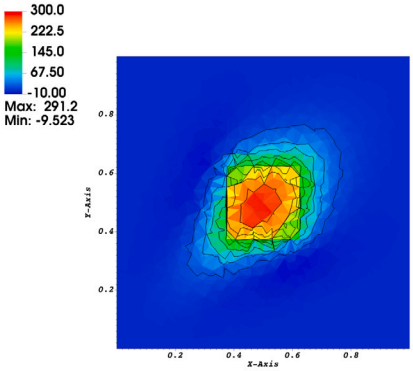

(c) Iterative E-MsCV solution.

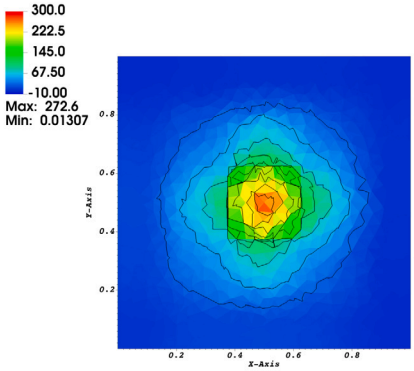

(d) MsRSB solution.

Fig. 15. The multiscale solutions for the heterogeneous and strongly anisotropic case using a structured background grid to generate the multiscale geometric entities. Slice at $z = 0.5$.

Table 6
The L_2 and L_∞ norms of the errors for the simulation of a reservoir containing a spherical fault under a channel configuration on a structured background grid.

Error (%)	MsCV	E-MsCV	Iterative E-MsCV	MsRSB	Iterative MsRSB
$\|\|u\|\|_2$	0.69	0.59	4×10^{-8}	0.61	4×10^{-8}
$\|\|u\|\|_\infty$	18.79	19.04	1×10^{-3}	17.80	3×10^{-3}

A similar effect is observed under a barrier configuration, as it can be seen in Figs. 21 and 22. The E-MsCV is able to recover the original solution to a reasonable degree and reproduce the barrier feature from the fine-scale solution. On the other hand, the 3-D extension of the MsCV diverges on those cases. Once again, the E-MsCV solutions are comparable to the MsRSB. From Tables 8 and 9 it is noticeable that the E-MsCV performs slightly better on a structured grid, but the oscillations on the unstructured counterpart produce a larger L_2 norm of the error when compared to the MsRSB.

Despite the errors introduced in the E-MsCV solution, the proposed iterative procedure was able to recover the original fine-scale MPFA-D reference solution to a very good degree of accuracy on both configurations, as seen in Figs. 19c, 20c, 21c and 22c. Specially with the unstructured background grid, the iterative procedure wiped the oscillations near the boundary of the domain. For these cases, a residual tolerance of 10^{-4} was used and it took just two iterations to achieve convergence. The computed errors presented in the Tables 6, 7, 8 and 9 further demonstrate the effectiveness of the procedure. It reduced the L_2 and L_∞ norms under a channel configuration to 10^{-8} and 10^{-3}, respectively. Similarly, for the barrier configuration, the L_2 and L_∞ norms are correspondingly of the order of 10^{-9} and 10^{-2}. Once again, we have run the procedure using the MsRSB operators and it was also able to recover the fine-scale MPFA-D solution.

6. Conclusions

In this paper, we have presented a 3-D extension of the Multiscale Control Volume (MsCV) method coupling it with the 3-D MPFA-D and the robust GLS interpolation for the simulation of single-phase flow in heterogeneous and anisotropic porous media,

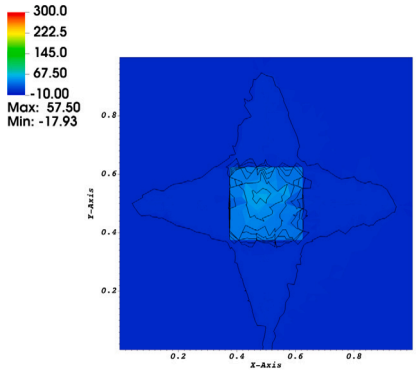

(a) MsCV solution.

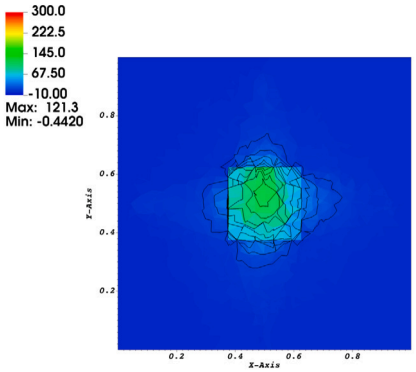

(b) E-MsCV solution.

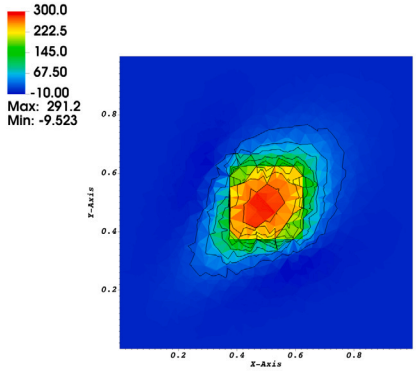

(c) Iterative E-MsCV solution.

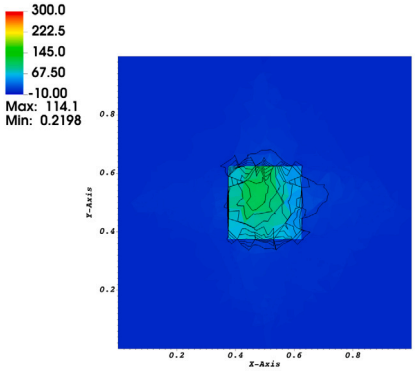

(d) MsRSB solution.

Fig. 16. The multiscale solutions for the heterogeneous and strongly anisotropic case using an unstructured background grid to generate the multiscale geometric entities. Slice at $z = 0.5$.

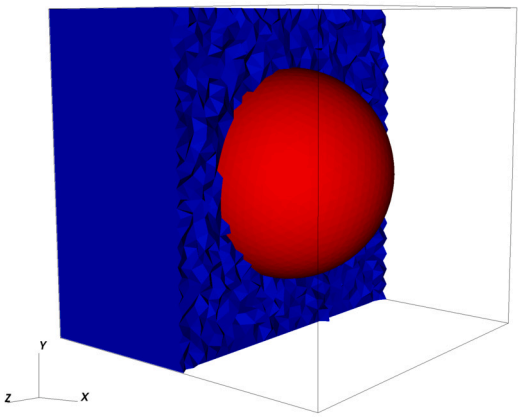

Fig. 17. The spherical fault region (red) within the reservoir.

Table 7
The L_2 and L_∞ norms of the errors for the simulation of a reservoir containing a spherical fault under a channel configuration on a unstructured background grid.

Error (%)	MsCV	E-MsCV	Iterative E-MsCV	MsRSB	Iterative MsRSB
$\|\|u\|\|_2$	2.00	3.62	4×10^{-8}	2.25	2×10^{-7}
$\|\|u\|\|_\infty$	33.87	49.30	1×10^{-3}	30.13	4×10^{-3}

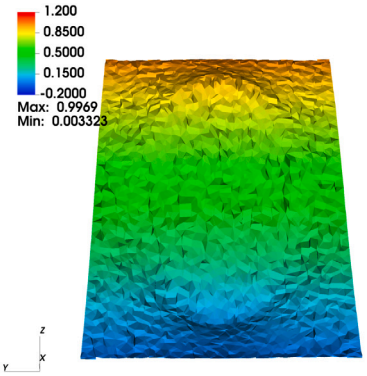

(a) Barrier configuration.

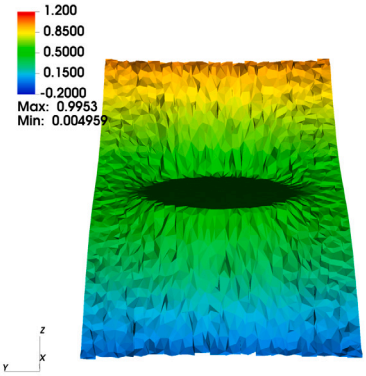

(b) Channel configuration.

Fig. 18. The fine-scale MPFA-D reference solutions for the single-phase simulation of a reservoir containing a spherical fault under a barrier (a) and channel (b) configuration. Slice at $y = 0$.

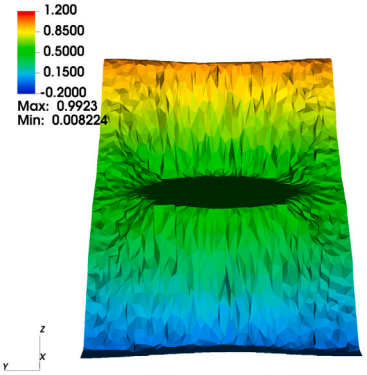

(a) MsCV solution

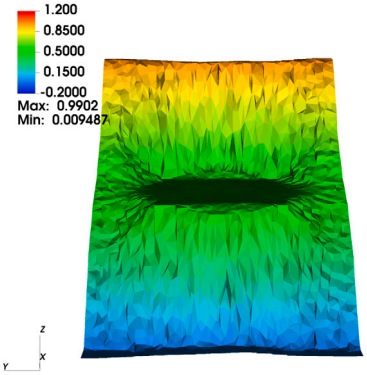

(b) E-MsCV solution.

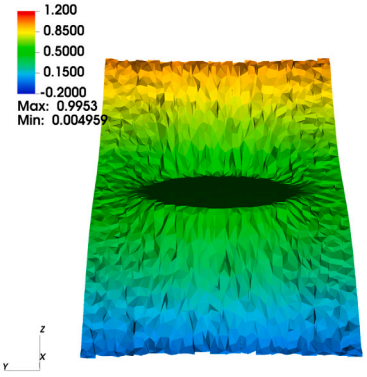

(c) Iterative E-MsCV.

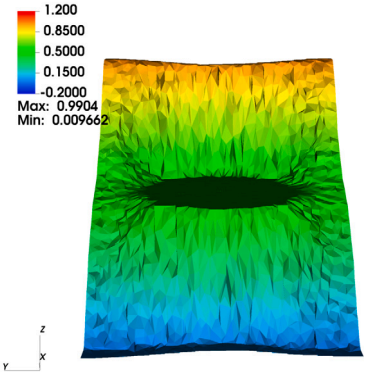

(d) MsRSB solution.

Fig. 19. The multiscale solutions under a channel configuration using a structured background grid. Slice at $z = 0$.

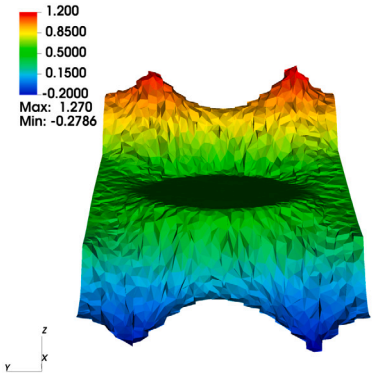

(a) MsCV solution

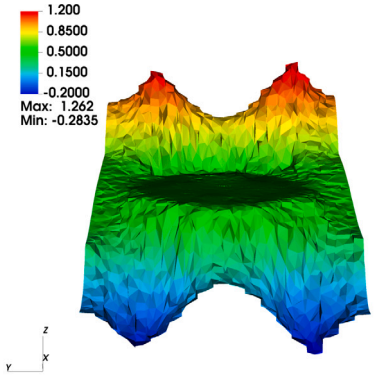

(b) E-MsCV solution.

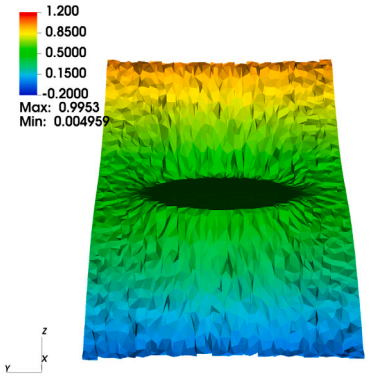

(c) Iterative E-MsCV.

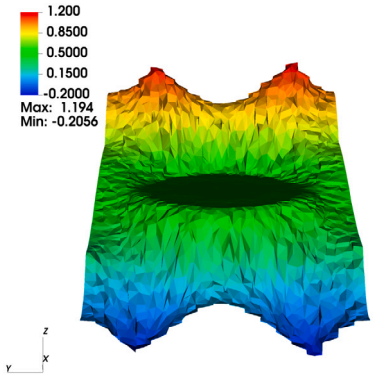

(d) MsRSB solution.

Fig. 20. The multiscale solutions under a channel configuration using an unstructured background grid. Slice at $z = 0$.

Table 8
The L_2 and L_∞ norms of the errors for the simulation of a reservoir containing a spherical fault under a barrier configuration on a structured background grid.

Error (%)	MsCV	E-MsCV	Iterative E-MsCV	MsRSB	Iterative MsRSB
$\|\|u\|\|_2$	7×10^8	0.39	5×10^{-9}	0.42	5×10^{-8}
$\|\|u\|\|_\infty$	5×10^7	10.43	0.02	27.33	0.03

Table 9
The L_2 and L_∞ norms of the errors for the simulation of a reservoir containing a spherical fault under a barrier configuration on a unstructured background grid.

Error (%)	MsCV	E-MsCV	Iterative E-MsCV	MsRSB	Iterative MsRSB
$\|\|u\|\|_2$	7×10^5	6.93	6×10^{-9}	1.33	4×10^{-6}
$\|\|u\|\|_\infty$	8×10^6	28.55	0.01	27.32	0.68

with the flexibility of been able of using either structured or unstructured grids in both scales. In addition, we have proposed an extension to 3-D geometries of the very flexible multiscale pre-processing algorithm by [30] based on the concept of a background grid and an enhanced version of the 3-D MsCV (E-MsCV) that incorporates the enhanced MsRSB preconditioning proposed by [18] to improve the convergence of the computation of the operators. Furthermore, we also extended and applied to a 3-D context the iterative procedure proposed by [41] and employed by [30]. From our experiments, the 3-D MsCV is capable of approximating the reference fine-scale solution to a good degree on low to intermediate complexity scenarios and the E-MsCV is able to converge on more challenging scenarios. By employing the additional iterative procedure, the fine-scale solution can be recovered to a very good degree with just a few iterations even in the presence of strong anisotropy or heterogeneities. It was also possible to notice that,

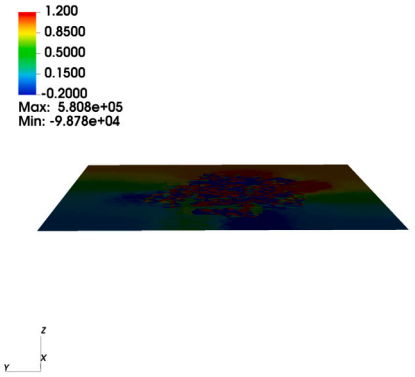

(a) MsCV solution

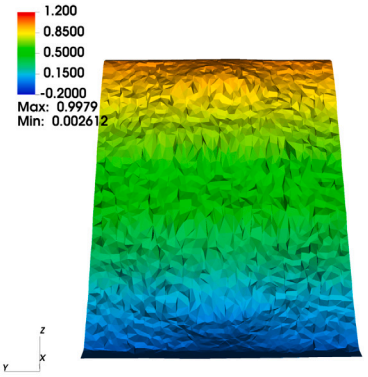

(b) E-MsCV solution.

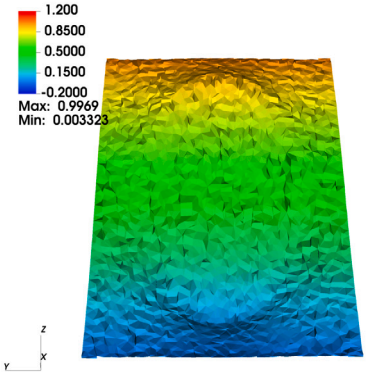

(c) Iterative E-MsCV.

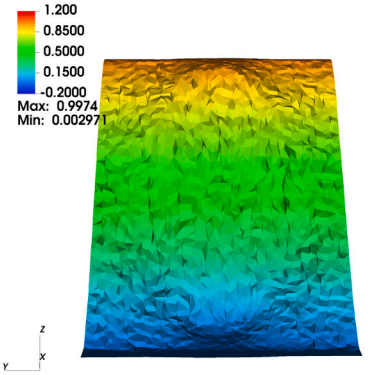

(d) MsRSB solution.

Fig. 21. The multiscale solutions under a barrier configuration using a structured background grid. Slice at $z = 0$.

despite of the robustness of the MPFA-D with the GLS interpolation, there are violations of the DMP which are exacerbated in the multiscale solution. In the near future, we intend to explore new approaches to generate the multiscale geometric entities under the background grid framework by adapting them to the underlying geological characteristics and to investigate algebraic multiscale strategies in place of the MsRSB. Furthermore, we also intend to address the DMP violation issue by introducing a defect correction scheme similar to the one proposed by [23,24] and to expand the work to the simulation of multiphase flows in heterogeneous and anisotropic porous media.

Declaration of competing interest

The authors declare the following financial interests/personal relationships which may be considered as potential competing interests: Paulo Roberto Maciel Lyra reports financial support was provided by Coordination for the Improvement of Higher Education Personnel (CAPES). Darlan Karlo Elisiario de Carvalho reports financial support was provided by Coordination for the Improvement of Higher Education Personnel (CAPES). Paulo Roberto Maciel Lyra reports financial support was provided by National Council for Scientific and Technological Development (CNPq). Darlan Karlo Elisiario de Carvalho reports financial support was provided by National Council for Scientific and Technological Development (CNPq). If there are other authors, they declare that they have no known competing financial interests or personal relationships that could have appeared to influence the work reported in this paper.

Data availability

Data will be made available on request.

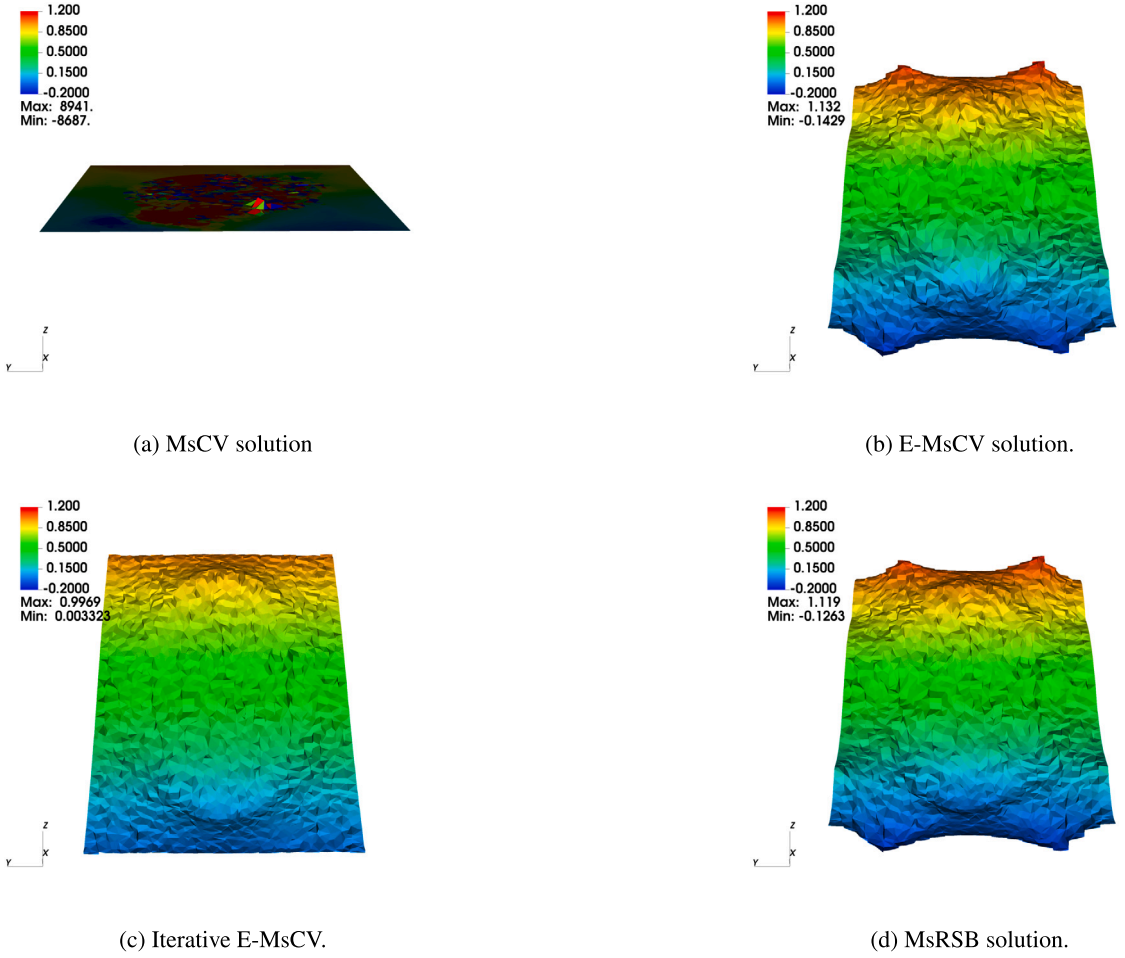

(a) MsCV solution

(b) E-MsCV solution.

(c) Iterative E-MsCV.

(d) MsRSB solution.

Fig. 22. The multiscale solutions under a barrier configuration using an unstructured background grid. Slice at $z = 0$.

Acknowledgements

The authors of this article would like to thank the support provided by the Coordination for the Improvement of Higher Education Personnel (CAPES), the National Council for Scientific and Technological Development (CNPq) under funding grants PQ-308334/2019-1 and PQ-310145/2021-0, and the Science Support Foundation of the State of Pernambuco (FACEPE) under funding grants IBPG-0017-3.01/18 and IBPG-0869-3.01/19.

References

[1] L. Li, A. Abushaikha, Joining the billion cell club: modelling of giant oil and gas fields using advanced simulation methods 2022 (2022) 1–3.
[2] A. Jaramillo, R.T. Guiraldello, S. Paz, R.F. Ausas, F.S. Sousa, F. Pereira, G.C. Buscaglia, Towards HPC simulations of billion-cell reservoirs by multiscale mixed methods, Comput. Geosci. 26 (2022) 481–501.
[3] Kabosu: Echelon software tackles complex field with flying colors, https://stoneridgetechnology.com/case-studies/kabosu-echelon-software-passes-complex-field-with-flying-colors/, 2022.
[4] C. Farmer, Upscaling: a review, Int. J. Numer. Methods Fluids 40 (2002) 63–78.
[5] Y. Efendiev, T.Y. Hou, Multiscale Finite Element Methods, Springer, 2009.
[6] P. Jenny, S. Lee, H. Tchelepi, Multi-scale finite-volume method for elliptic problems in subsurface flow simulation, J. Comput. Phys. 187 (2003) 47–67.
[7] I. Lunati, P. Jenny, Multiscale finite-volume method for compressible multiphase flow in porous media, J. Comput. Phys. 216 (2006) 616–636.
[8] S.H. Lee, C. Wolfsteiner, H.A. Tchelepi, Multiscale finite-volume formulation for multiphase flow in porous media: black oil formulation of compressible, three-phase flow with gravity, Comput. Geosci. 12 (2008) 351–366.
[9] H. Zhou, H.A. Tchelepi, Operator-based multiscale method for compressible flow, SPE J. 13 (2008) 267–273.
[10] H. Zhou, H.A. Tchelepi, Two-stage algebraic multiscale linear solver for highly heterogeneous reservoir models, in: SPE Reservoir Simulation Conference, 2011, pp. SPE-141473-MS.
[11] S. Verma, K. Aziz, A control volume scheme for flexible grids in reservoir simulation, in: SPE Reservoir Simulation Conference, 1997, pp. SPE-37999-MS.
[12] O. Møyner, K.-A. Lie, The multiscale finite-volume method on stratigraphic grids, SPE J. 19 (2014) 816–831.
[13] O. Møyner, K.-A. Lie, A multiscale two-point flux-approximation method, J. Comput. Phys. 275 (2014) 273–293.
[14] A.C.R. Souza, L.M.C. Barbosa, F.R.L. Contreras, P.R.M. Lyra, D.K.E. de Carvalho, A multiscale control volume framework using the multiscale restriction smooth basis and a non-orthodox multi-point flux approximation for the simulation of two-phase flows on truly unstructured grids, J. Pet. Sci. Eng. 188 (2020) 106851.

[15] E. Parramore, M.G. Edwards, M. Pal, S. Lamine, Multiscale finite-volume CVD-MPFA formulations on structured and unstructured grids, Multiscale Model. Simul. 14 (2016) 559–594.
[16] O. Møyner, K.-A. Lie, A multiscale restriction-smoothed basis method for high contrast porous media represented on unstructured grids, J. Comput. Phys. 304 (2016) 46–71.
[17] Ø.S. Klemetsdal, O. Møyner, K.-A. Lie, Accelerating multiscale simulation of complex geomodels by use of dynamically adapted basis functions, Comput. Geosci. 24 (2020) 459–476.
[18] S.B. Bosma, S. Klevtsov, O. Møyner, N. Castelletto, Enhanced multiscale restriction-smoothed basis (MsRSB) preconditioning with applications to porous media flow and geomechanics, J. Comput. Phys. 428 (2021) 109934.
[19] Z. Gao, J. Wu, A linearity-preserving cell-centered scheme for the heterogeneous and anisotropic diffusion equations on general meshes, Int. J. Numer. Methods Fluids 67 (2011) 2157–2183.
[20] F. Contreras, P. Lyra, M. Souza, D. Carvalho, A cell-centered Multipoint Flux Approximation method with a diamond stencil coupled with a higher order finite volume method for the simulation of oil–water displacements in heterogeneous and anisotropic petroleum reservoirs, Comput. Fluids 127 (2016) 1–16.
[21] I. Aavatsmark, T. Barkve, O. Bøe, T. Mannseth, Discretization on unstructured grids for inhomogeneous, anisotropic media. Part I: derivation of the methods, SIAM J. Sci. Comput. 19 (1998) 1700–1716.
[22] I. Aavatsmark, T. Barkve, O. Bøe, T. Mannseth, Discretization on unstructured grids for inhomogeneous, anisotropic media. Part II: discussion and numerical results, SIAM J. Sci. Comput. 19 (1998) 1717–1736.
[23] T.M. Cavalcante, R.J.M.L. Filho, A.C.R. Souza, D.K.E. Carvalho, P.R.M. Lyra, A Multipoint Flux Approximation with a diamond stencil and a non-linear defect correction strategy for the numerical solution of steady state diffusion problems in heterogeneous and anisotropic media satisfying the discrete maximum principle, J. Sci. Comput. 93 (2022) 42.
[24] A.C.R. de Souza, D.K.E. de Carvalho, T. de Moura Cavalcante, F.R. Licapa Contreras, M.G. Edwards, P.R.M. Lyra, A nonlinear repair technique for the MPFA-D scheme in single-phase flow problems and heterogeneous and anisotropic media, J. Comput. Phys. 501 (2024) 112759.
[25] F.R.L. Contreras, M.R.A. Souza, P.R.M. Lyra, D.K.E. Carvalho, A MPFA method using harmonic points coupled to a multidimensional optimal order detection method (MOOD) for the simulation of oil-water displacements in petroleum reservoirs, Rev. Interdiscip. Pesqui. Eng. 2 (2017) 76–95.
[26] F.R. Contreras, P.R. Lyra, D.K. de Carvalho, A new Multipoint Flux Approximation method with a quasi-local stencil (MPFA-QL) for the simulation of diffusion problems in anisotropic and heterogeneous media, Appl. Math. Model. 70 (2019) 659–676.
[27] R.J. de Lira Filho, S.R. dos Santos, T. de, M. Cavalcante, F.R. Contreras, P.R. Lyra, D.K. de Carvalho, A linearity-preserving finite volume scheme with a diamond stencil for the simulation of anisotropic and highly heterogeneous diffusion problems using tetrahedral meshes, Comput. Struct. 250 (2021) 106510.
[28] C. Dong, T. Kang, A least squares based diamond scheme for 3D heterogeneous and anisotropic diffusion problems on polyhedral meshes, Appl. Math. Comput. 418 (2022) 126847.
[29] T. de Moura Cavalcante, Simulation of Immiscible Two-Phase Flow in 3-D Naturally Fractured Reservoirs Using a Locally Conservative Method, a Projection-Based Embedded Discrete Fracture Model and Unstructured Tetrahedral Meshes, Ph.D. thesis, Universidade Federal de Pernambuco, 2023.
[30] A.C.R. de Souza, D.K.E. de Carvalho, J.C.A. dos Santos, R.B. Willmersdorf, P.R.M. Lyra, M.G. Edwards, An algebraic multiscale solver for the simulation of two-phase flow in heterogeneous and anisotropic porous media using general unstructured grids (AMS-U), Appl. Math. Model. 103 (2022) 792–823.
[31] H. Hajibeygi, G. Bonfigli, M.A. Hesse, P. Jenny, Iterative multiscale finite-volume method, J. Comput. Phys. 227 (2008) 8604–8621.
[32] I. Lunati, M. Tyagi, S.H. Lee, An iterative multiscale finite volume algorithm converging to the exact solution, J. Comput. Phys. 230 (2011) 1849–1864.
[33] M. Borsuk, V. Kondratiev, Chapter 5 - the Dirichlet problem for elliptic linear divergent equations in a nonsmooth domain, in: M. Borsuk, V. Kondratiev (Eds.), Elliptic Boundary Value Problems of Second Order in Piecewise Smooth Domains, in: North-Holland Mathematical Library, vol. 69, Elsevier, 2006, pp. 165–213.
[34] L. Véron, CHAPTER 8 - elliptic equations involving measures, in: M. Chipot, P. Quittner (Eds.), Handbook of Differential Equations: Stationary Partial Differential Equations, in: Handbook of Differential Equations: Stationary Partial Differential Equations, vol. 1, North-Holland, 2004, pp. 593–712.
[35] M. Pal, M.G. Edwards, A family of multi-point flux approximation schemes for general element types in two and three dimensions with convergence performance, Int. J. Numer. Methods Fluids 69 (2012) 1797–1817.
[36] M.G. Edwards, H. Zheng, A quasi-positive family of continuous Darcy-flux finite-volume schemes with full pressure support, J. Comput. Phys. 227 (2008) 9333–9364.
[37] L.M.C. Barbosa, A.R.E. Antunes, P.R.M. Lyra, D.K.E. Carvalho, An iterative modified multiscale control volume method for the simulation of highly heterogeneous porous media flow, J. Braz. Soc. Mech. Sci. Eng. 40 (2018).
[38] Y. Wang, H. Hajibeygi, H.A. Tchelepi, Algebraic multiscale solver for flow in heterogeneous porous media, J. Comput. Phys. 259 (2014) 284–303.
[39] Y. Saad, Iterative Methods for Sparse Linear Systems, 2. ed., Society for Industrial and Applied Mathematics, 2003.
[40] G. Karypis, V. Kumar, A fast and high quality multilevel scheme for partitioning irregular graphs, SIAM J. Sci. Comput. 20 (1998) 359–392.
[41] S. Bosma, H. Hajibeygi, M. Tene, H.A. Tchelepi, Multiscale finite volume method for discrete fracture modeling on unstructured grids (MS-DFM), J. Comput. Phys. 351 (2017) 145–164.
[42] Z. Mehrdoost, Unstructured grid adaptation for multiscale finite volume method, Comput. Geosci. 23 (2019) 1293–1316.
[43] J.E. Aarnes, S. Krogstad, K.-A. Lie, Multiscale mixed/mimetic methods on corner-point grids, Comput. Geosci. 12 (2008) 297–315.
[44] K.-A. Lie, O. Møyner, J.R. Natvig, Use of multiple multiscale operators to accelerate simulation of complex geomodels, SPE J. 22 (2017) 1929–1945.
[45] R. Eymard, G. Henry, R. Herbin, F. Hubert, R. Klöfkorn, G. Manzini, 3d benchmark on discretization schemes for anisotropic diffusion problems on general grids, in: J. Fořt, J. Fürst, J. Halama, R. Herbin, F. Hubert (Eds.), Finite Volumes for Complex Applications VI Problems & Perspectives, Springer, Berlin Heidelberg, Berlin, Heidelberg, 2011, pp. 895–930.
[46] C.R. Dohrmann, O.B. Widlund, An overlapping Schwarz algorithm for almost incompressible elasticity, SIAM J. Numer. Anal. 47 (2009) 2897–2923.
[47] A. Heinlein, A. Klawonn, J. Knepper, O. Rheinbach, Multiscale coarse spaces for overlapping Schwarz methods based on the ACMS space in 2D, ETNA, Electron. Trans. Numer. Anal. 48 (2018) 156–182.
[48] M.G. Edwards, H. Zheng, Quasi M-matrix multifamily continuous Darcy-flux approximations with full pressure support on structured and unstructured grids in three dimensions, SIAM J. Sci. Comput. 33 (2011) 455–487.